REPORT DOCUMENTATION PAGE

Form Approved
OMB No. 0704-0188

The public reporting burden for this collection of information is estimated to average 1 hour per response, including the time for reviewing instructions, searching existing data sources, gathering and maintaining the data needed, and completing and reviewing the collection of information. Send comments regarding this burden estimate or any other aspect of this collection of information, including suggestions for reducing the burden, to Department of Defense, Washington Headquarters Services, Directorate for Information Operations and Reports (0704-0188), 1215 Jefferson Davis Highway, Suite 1204, Arlington, VA 22202-4302. Respondents should be aware that notwithstanding any other provision of law, no person shall be subject to any penalty for failing to comply with a collection of information if it does not display a currently valid OMB control number.
PLEASE DO NOT RETURN YOUR FORM TO THE ABOVE ADDRESS.

1. REPORT DATE *(DD-MM-YYYY)*	2. REPORT TYPE	3. DATES COVERED *(From - To)*
	Final Report	15 March 2005 - 31 December 2005

4. TITLE AND SUBTITLE

Coherent Ion Acceleration Using Beating Electrostatic Waves

5a. CONTRACT NUMBER

5b. GRANT NUMBER

FA9550-05-1-0181

5c. PROGRAM ELEMENT NUMBER

6. AUTHOR(S)

Professor Edgar Choueiri

5d. PROJECT NUMBER

5e. TASK NUMBER

5f. WORK UNIT NUMBER

7. PERFORMING ORGANIZATION NAME(S) AND ADDRESS(ES)

Applied Physics Group
Princeton University
Princeton NJ 08544

8. PERFORMING ORGANIZATION REPORT NUMBER

9. SPONSORING/MONITORING AGENCY NAME(S) AND ADDRESS(ES)

USAF/AFRL
AFOSR
875 North Randolph Street
Arlington VA 22203
Dr. Mitat Birkan

10. SPONSOR/MONITOR'S ACRONYM(S)

AFOSR

11. SPONSOR/MONITOR'S REPORT NUMBER(S)

AFRL-SR-AR-TR-06-0282

12. DISTRIBUTION/AVAILABILITY STATEMENT

Distribution Statement A. Approved for public release; distribution is unlimited.

13. SUPPLEMENTARY NOTES

14. ABSTRACT

In this final technical report we document, in three chapters and an appendix, the results obtained under the 1-year continuation AFOSR contract (FA9550-05-1-0181; Start date: 03/15/05; End date: 12/31/05) to our AFOSR-sponsored study of a new ion acceleration mechanism using beating electrostatic waves.
The first phase of the work (F49620-02-1-0009; State date: 08/31/2002; End date: 9/1/04) was documented in detail in a final report submitted to AFOSR on 1/24/05. In that report we documented the work on, and results from, our theoretical investigation of the problem and presented preliminary experimental work aimed at demonstrating and studying the new effect in the laboratory. In this present report we document the final experimental results and related studies, undertaken during the 1-year continuation of the project under AFOSR contract FA9550-05-1-0181.

15. SUBJECT TERMS

16. SECURITY CLASSIFICATION OF:			17. LIMITATION OF ABSTRACT	18. NUMBER OF PAGES	19a. NAME OF RESPONSIBLE PERSON
a. REPORT	b. ABSTRACT	c. THIS PAGE			19b. TELEPHONE NUMBER *(Include area code)*
U	U	U	UU	51 ~~31~~	

Coherent Ion Acceleration Using Beating Electrostatic Waves

FINAL REPORT
to the US Air Force Office of Scientific Research

GRANT NUMBER: FA9550-05-1-0181
Project Period: March 15, 2005 - December 31, 2005

PI: Prof. Edgar Choueiri

Graduate Student: Rostislav Spektor

Electric Propulsion and Plasma Dynamics Lab (EPPDyL)
Applied Physics Group
MAE Dept., Princeton University
Princeton NJ 08544
Phone: (609) 258 5220 Fax: (609) 258 6875
E-mail: choueiri@princeton.edu

20060816083

Contents

1 Experimental Setup and Diagnostics **6**
- 1.1 Vacuum Chamber 6
- 1.2 Plasma Source 9
- 1.3 Electrostatic (ES) Wave Antennas 12
  - 1.3.1 Two-plate ES Antenna 13
  - 1.3.2 Loop ES Antenna 15
  - 1.3.3 Beating Waves – Mixing Signals from Two Sources 15
- 1.4 Diagnostics 15
  - 1.4.1 Langmuir Probes 17
  - 1.4.2 Electron Temperature and Plasma Density Measurements . . . 19
  - 1.4.3 Dispersion Relation Measurements 20
  - 1.4.4 Laser Induced Fluorescence 22
  - 1.4.5 LIF Theory 22
  - 1.4.6 LIF Implementation 22
  - 1.4.7 LIF Instrumentation 24
- 1.5 Operation and Procedures 27

2 Experimental Results and Analysis **28**
- 2.1 Wave Detection 29
- 2.2 Dispersion Relation Measurements 32
- 2.3 Effects of Ion-Neutral Collisions 34
- 2.4 Ion Heating in the BWX 36
- 2.5 Final Remarks 41

3 Conclusions **42**
- 3.1 Summary of Major Findings 42
  - 3.1.1 Theoretical Findings 42
  - 3.1.2 Numerical Findings 43
  - 3.1.3 Experimental Findings 43
- 3.2 Recommendations for Future Work 44

A ES Dispersion for a Homogeneous, Isotropic, Magnetized, Collisional Plasma 46

2

Bibliography **48**

SYNOPSIS

In this final technical report we document, in three chapters and an appendix, the results obtained under the 1-year continuation AFOSR contract (FA9550-05-1-0181; Start date: 03/15/05; End date:12/31/05) to our AFOSR-sponsored study of a new ion acceleration mechanism using beating electrostatic waves.

The first phase of the work (F49620-02-1-0009; Start date: 08/31/02; End date:9/1/04) was documented in detail in a final report submitted to AFOSR on 1/24/05. In that report we documented the work on, and results from, our theoretical investigation of the problem and presented preliminary experimental work aimed at demonstrating and studying the new effect in the laboratory. In this present report we document the final experimental results and related studies, undertaken during the 1-year continuation of the project under AFOSR contract A9550-05-1-0181.

Background Unlike previously known methods of energizing plasmas with electrostatic waves, and which accelerate only ions whose initial velocities are above a certain threshold (close to the wave's velocity), the new mechanism can accelerate ions with arbitrarily small initial velocities (as illustrated in Fig. (1)). This results in significant improvements to the acceleration/heating efficiency (by as much as 45%) over previous techniques. The benefits to the state of the art of space propulsion stem from the high efficiency of the new mechanism, its thersholdless nature and its capabilities of producing high ion energies and its electrodeless character. These advantages have been discussed in detail in the final report for the previous AFOSR contract.

The goal of this fundamental study was to improve the theoretical understanding of a new ion acceleration mechanism based on beating electrostatic waves (BEW) through analytical and numerical investigations, and to demonstrate ion heating by BEW for the first time in a laboratory environment in order to establish its basic relevance for space propulsion.

Summary from Previous Report Under the previous AFOSR contract (F49620-02-1-0009) we did the following:

1. Demonstrated theoretically that a new highly ion acceleration mechanism by beating electrostatic (ES) waves, whose high ion acceleration efficiency renders it particularly relevant to space propulsion, is real and is a fundamental phenomenon that occurs only under specific conditions that were not known before. We derived, from first principles, the fundamental necessary *and* sufficient conditions for the acceleration mechanism to occur.

2. We studied using Monte Carlo simulations the effects of collisions (that would occur in a real low temperature plasma) on the ion acceleration mechanism and found that collisions can enhance the effects due to scattering of ions out of the forbidden region of phase space.

3. We designed and constrducted a dedicated experiment to study the new ion acceleration mechanism. We were able to launch and beat ion cyclotron waves in

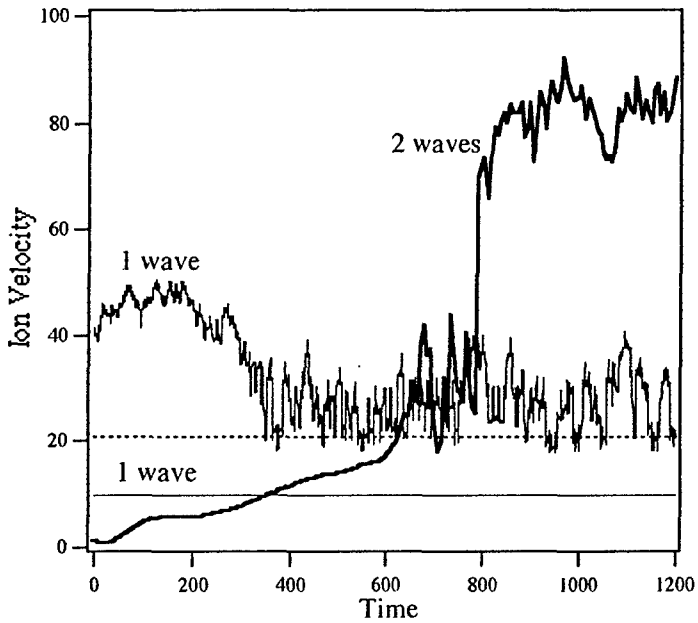

Figure 1: Calculation from first principles (using Hamiltonian formulation) of ion acceleration by two beating electrostatic waves (red curve) compared to the effect of a single wave (blue curve). Unlike the single wave case, the 2-wave interaction accelerates ions whose initial velocity is below the classical threshold (dotted horizontal line) to significantly high velocities. The thresholdless nature and efficiency of this acceleration mechanism make it most promising for propulsion applications. More detail is given in the the final report for the previous AFOSR contract.

an argon plasma produced by a helicon source and, using a dedicated state-of-the-art LIF diagnostic system (acquired through a recent DURIP grant), we were able to provide a preliminary laboratory demonstration of the existence of this new ion acceleration mechanism.

Summary of Present Report In the present report we document the work accomplished under a 1-year continuation contract from AFOSR (FA9550-05-1-0181) which aimed at a detailed experimental demonstration of the existence of this effect and a characterization of its ability to provide ion acceleration that is significantly more efficient than standard (non-beating) wave acceleration of ions.

In particular, we document an experimental study of ion heating by beating electrostatic ion cyclotron (EIC) waves in a magnetized, radio-frequency sustained plasma.

Ion heating up to 35% was observed in the presence of the EIC waves excited by a two-plate antenna. It was found that ion-neutral collisions significantly damp the

backward branch of the EIC wave, which is most effective in coupling with ions. Thus, ion-neutral collisions indirectly play a detrimental role in the heating mechanism. Despite the damping effects of such collisions, it was shown that the beating electrostatic waves can heat ions to a higher temperature than a single electrostatic wave. This enhancement in ion temperature was found to be 15% for the particular conditions of the reported experiment, but is expected to be significantly higher in a less collisional, or equivalently hotter, plasma. This finding supports the theoretical prediction that beating waves can produce more efficient heating by interacting with ions below the single-wave velocity threshold.

Chapter 1

Experimental Setup and Diagnostics

This chapter presents a detailed description of the BWX (Beating Waves Experiment) apparatus and diagnostics used to study the electrostatic wave propagation and dispersion, as well as the resulting stochastic ion heating. The chapter is organized as follows. First, we give a detailed description of the vacuum chamber in Section 1.1 and the rf plasma source in Section 1.2. Section 1.3 describes various electrostatic (ES) antennas that were tried in order to excite the electrostatic waves. Section 1.4 is dedicated to the diagnostics. It describes the various Langmuir probes and the LIF apparatus used to measure the plasma and wave properties.

1.1 Vacuum Chamber

A technical drawing and computer rendering of the Beating Waves Experiment (BWX) are shown in Fig. 1.1 and Fig. 1.2. The BWX vacuum chamber consists of a 6 cm diameter and 37 cm long Pyrex cylinder serving as the plasma source, connected through an aluminum plate to a 20 cm and 46 cm long Pyrex cylinder serving as the test section. The aluminum plate is electrically isolated from the rest of the chamber and the electromagnet. The small cylinder is capped with a molybdenum backplate, which is electrically floating to minimize sputtering. The vacuum chamber is placed inside an electromagnet, which produces a homogeneous, steady-state magnetic field up to 0.1 Tesla, that is uniformly axial throughout the test section. The axial magnetic field along the centerline is shown in Fig. 1.3. The two curves correspond to ion cyclotron frequency of 10 kHz and 30 kHz in the test section of the vacuum chamber. Pressure of 1 to 30 mTorr is typically maintained by a gas feed (Ar or He) at the aluminum endplate of the large cylinder and by a 150 l/s turbo pump with a conductance controller backed up by a roughing pump. The system is capable of maintaining a base pressure of $2 \cdot 10^{-6}$ Torr.

Once the discharge is ignited in the small cylinder, the plasma propagates along the magnetic field lines, which are parallel to the axis of the cylinders, into the large

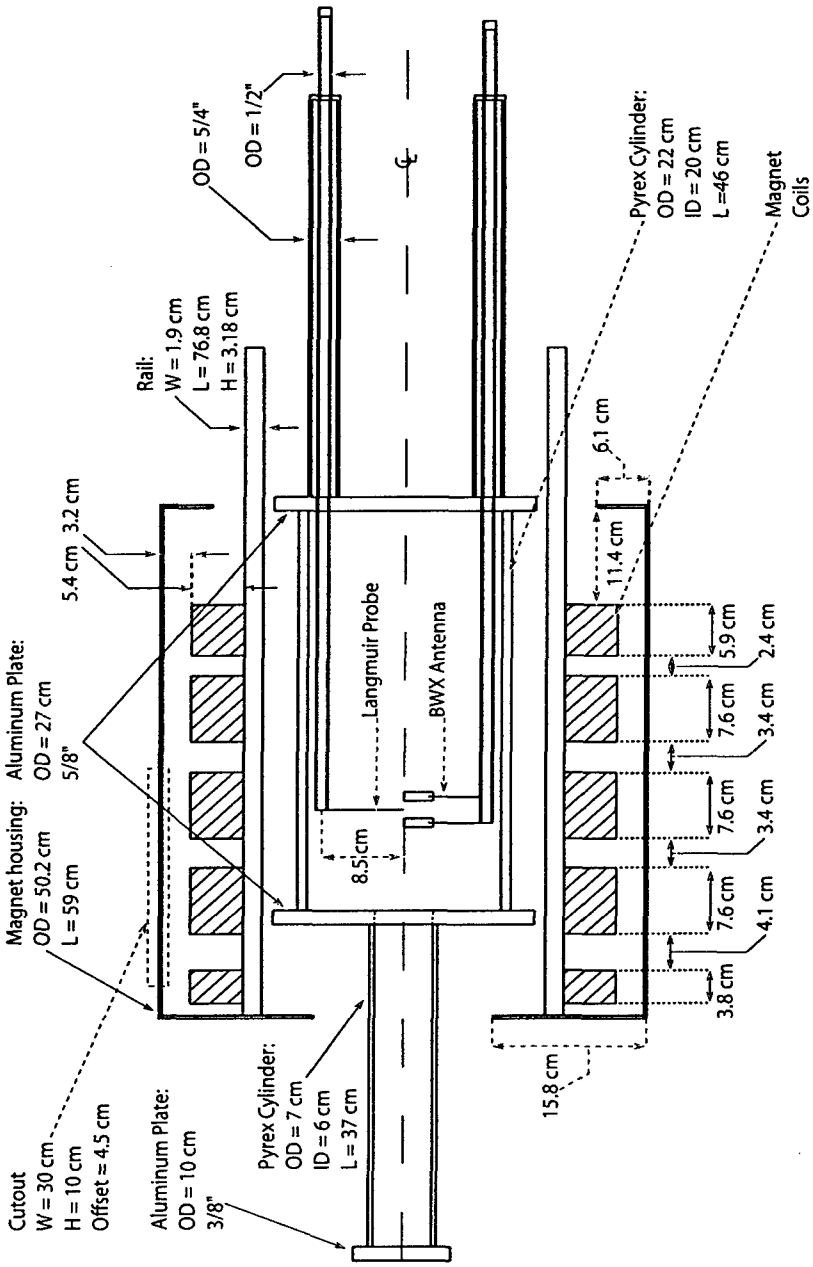

Figure 1.1: Schematic of the BWX vacuum chamber.

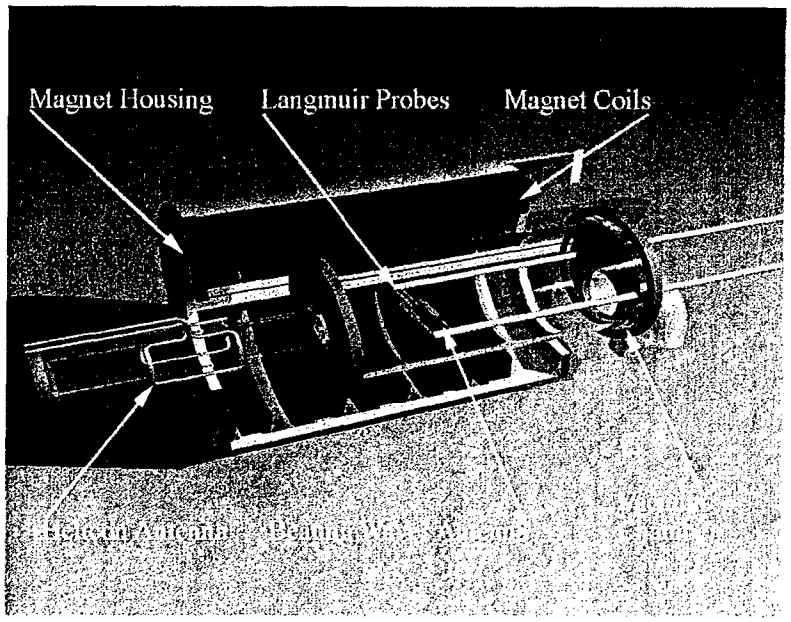

Figure 1.2: Computer rendering showing how the components of the BWX apparatus fit together.

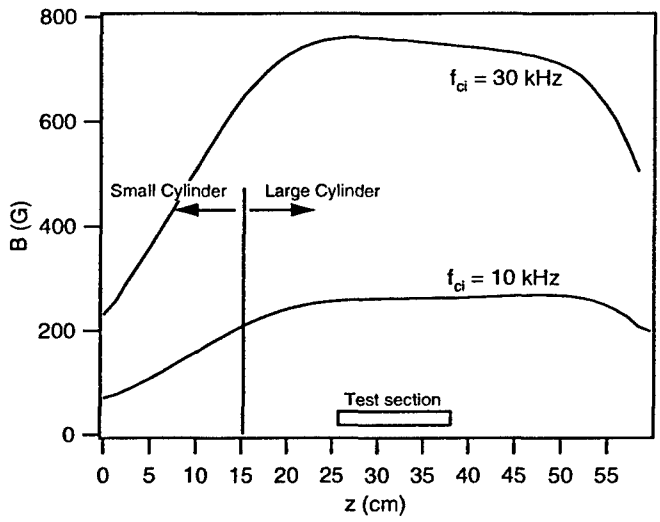

Figure 1.3: Axial magnetic field B_z along the centerline of the magnet. The ion cyclotron frequency varies by less than 3% within the test section of the large chamber, where the electrostatic waves are launched.

chamber where the wave-launching and plasma-heating experiments are conducted.

1.2 Plasma Source

The plasma is generated in the smaller cylinder by a helicon source consisting of a Boswell saddle-type rf antenna wrapped around the smaller Pyrex cylinder, as shown in Fig. 1.4. The helicon antenna is made of 0.25" copper tubbing to allow water cooling. The discharge is produced by supplying rf power to the helicon antenna from an ENI 13.56 MHz 1.2 kW power supply through a tuner. The tuner, shown in Fig. 1.5, consists of an L network made of two Jennings 1000 pF 3 kV variable vacuum capacitors. The tuner is placed as close to the helicon antenna as possible to maximize coupling to the antenna. A power control circuit allows for pulsed as well as steady-state plasma generation. The vacuum chamber is incased in a Faraday cage consisting partly of the magnet casing and partly of copper mesh to prevent the radiation emitted by the helicon antenna from leaking into the laboratory. The shielding is shown in Fig. 1.4.

A power control circuit allows for pulsed as well as steady-state plasma generation. The circuit consists of an HP 8116A function generator that sends a control and trigger signals to the ENI RF power supply. In addition, the signal from the HP function generator is delivered to a digital pulse and delay generator (DDG) DG565, where the signal can be delayed by an arbitrary amount to trigger the ES antennas, Langmuir probes, or other diagnostics.

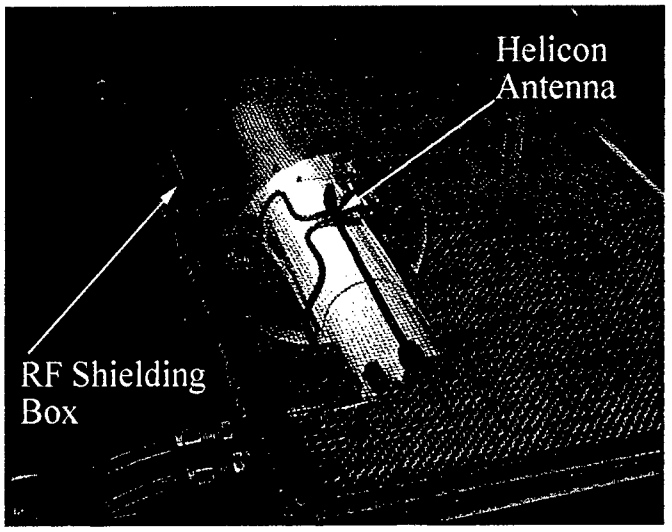

Figure 1.4: Photograph of an inductive rf discharge established by the helicon antenna. The copper mesh box surrounding the vacuum chamber forms a safety rf shielding cage.

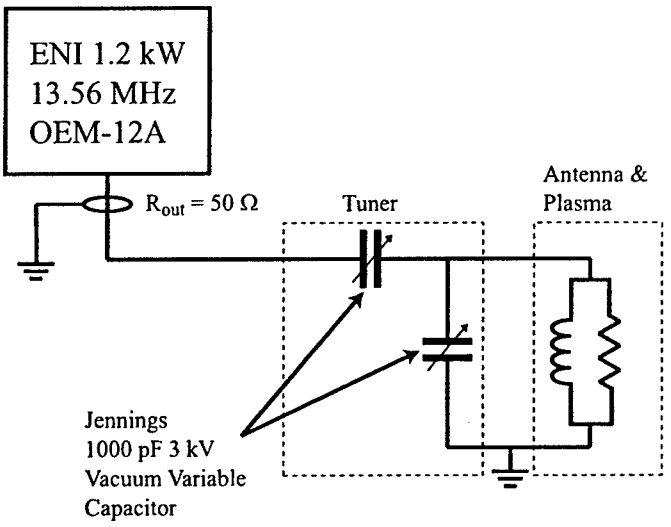

Figure 1.5: Schematic of the electric circuit driving the helicon antenna. An ENI OEM-12A 13.56 MHz rf power supply provides up to 1.2 kW to the helicon antenna through a π-network tuner consisting of two Jennings 1000 pF 3 kV variable vacuum capacitors.

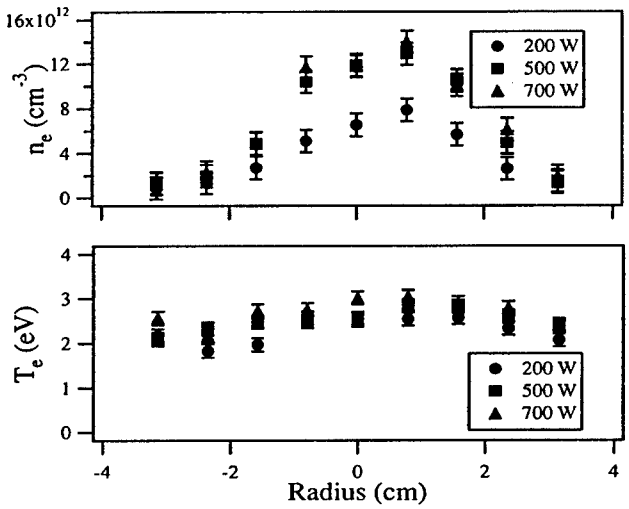

Figure 1.6: Plasma density and electron temperature profiles for various rf power to the helicon antenna. Plasma density increases with rf power. Electron temperature, on the other hand, is not a strong function of the rf power. Helicon discharge is observed as the rf power is raised beyond 500W. B=261 Gauss, P=1mTorr.

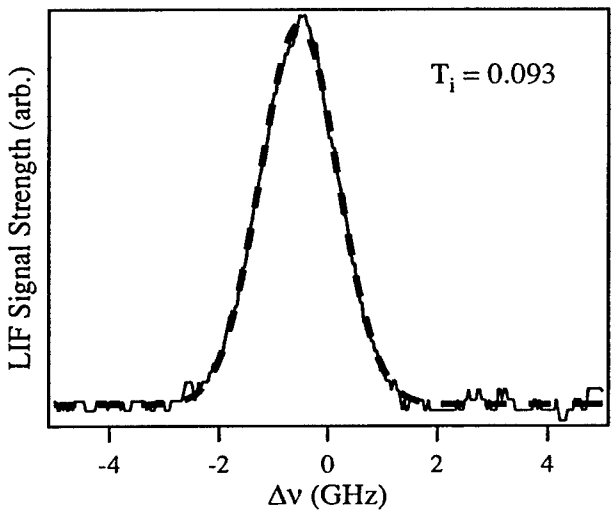

Figure 1.7: Typical LIF signal strength profile measured in the BWX experiment. The thin line is obtained from ~300 LIF data points, while the thick dashed line (almost indistinguishable) is a Gaussian fit to the data points.

An inductive discharge is easily obtained with only a few watts of forward rf power to the helicon antenna and only a few percent of rf power reflected. A helicon discharge with high plasma density ($n_e = 10^{13}$ cm^{-3}) can be produced as rf power to the helicon antenna is raised above 500 W by properly adjusting pressure, magnetic field, and capacitance of the coupling tuner. The inductively coupled discharge looks homogeneous and occupies the entire cross-section of the small cylinder. When the helicon discharge is obtained with argon, a bright blue column can be observed at the centerline. Measured radial profiles of plasma density and electron temperature for both types of discharges are shown in Fig. 1.6. The radial distribution of the plasma density depends on the power input from the helicon antenna. For the low-power discharges the profile is more uniform, while at higher rf powers the profile becomes peaked at the center of the plasma column. The electron temperature, on the other, hand displays a more uniform profile, and is much less sensitive to the helicon antenna power. A small asymmetry in both plasma density and electron temperature profiles is most likely due to the interaction between the Langmuir probe and the plasma column.

An example of the ion velocity distribution function measured by the LIF technique is shown in Fig. 1.7. The distribution profile is obtained by scanning the laser through ~300 different frequencies. The ion temperature can be determined from a Gaussian fit to the measured velocity distribution profile. This technique will be further explained in Section 1.4.5. An excellent agreement between the fit (thick dashed line) and the measured distribution (thin line) indicates that the accuracy of the ion temperature measurement is determined primarily by the shot-to-shot repeatability rather than the fit accuracy. For the experiments reported here, the background electron and ion (perpendicular) temperatures were $T_e \approx 3$ eV and $T_{i\perp} \approx 0.1$ eV, and the ratio of the ion-neutral charge-exchange collision frequency to the ion cyclotron frequency $\nu_{ex}/\omega_{ci} = 0.2$, as will be shown in the next section. The parallel ion temperature was not measured, but in a typical inductive discharge it roughly equals half of the perpendicular ion temperature. It should be noted that the ratio ν_{ex}/ω_{ci} is an order of magnitude above that of the Skiff's experiment [1]. While the ion-neutral collision frequency is an order of magnitude smaller than the ion cyclotron frequency, charge-exchange collisions play an important role in the electrostatic wave dispersion. Figure 1.8 shows the range of some natural plasma frequencies in the BWX that were calculated with the measured T_e, T_i, n_e, and B_0.

1.3 Electrostatic (ES) Wave Antennas

In order to launch electrostatic waves into the plasma three different electrostatic (ES) antenna types were tested: 1) Helmholtz-coil antenna wrapped outside the vacuum chamber, 2) internal (to the vacuum chamber) two-plate antenna, and 3) internal loop antenna. We were unable to launch electrostatic waves with the Helmholtz-coil antenna. Therefore, in this report we will concentrate on the other two antenna types. The two-plate or loop antennas were placed inside the test section of the BWX vacuum chamber. In addition, the two-plate ES antenna was situated directly inside the plasma column. The ES antennas were driven by one or two Wavetek 180 signal generators, which are capable of producing a signal up to 20 V_{pp} into a 50Ω load. The signal was

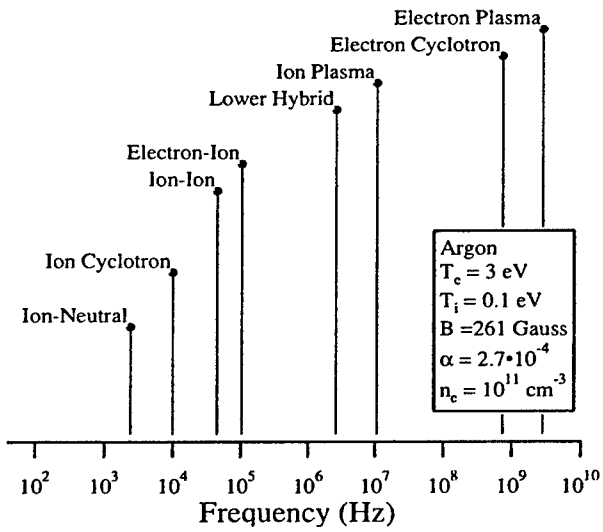

Figure 1.8: Typical plasma parameters for the BWX experiment calculated with measured T_e, T_i, n_e, and B.

further amplified by an operational amplifier or an ENI 2100L broadband amplifier, and sent through a tuning circuit to match the ES antenna impedance.

1.3.1 Two-plate ES Antenna

The two-plate ES antenna has been previously used to launch a single electrostatic wave above the ion cyclotron frequency by Goree *et al.* in the toroidal ACT-1 device [2, 3], and by Skiff *et al.* in a linear device [1]. The two-plate ES antenna used in the BWX experiment is similar to the one used in these experiments, and is constructed from two 1 cm × 6 cm molybdenum plates placed ~3 cm apart along the magnetic field lines. The plates are oriented such that the long side and the surface normal are perpendicular to the center axis of the vacuum chamber (and the magnetic field), as shown in Fig. 1.9. The plates are attached to a movable arm that can rotate the ES antenna in and out of the plasma column, and is also free to move along the axis of the vacuum chamber. The plates could be electrically driven in or out of phase with each other by a circuit schematically illustrated in Fig. 1.10. To drive the ES antenna in phase, a coupling capacitor ($C_c = 2\mu F$) can be used to allow both plates to float with respect to the plasma potential. To drive the plates out of phase, the ES antenna is connected through a 1:1 transformer. When the plates are driven out of phase, the parallel wavenumber is controlled by the plate spacing, and when the plates are driven in phase, the parallel wavelength is determined by the vacuum chamber geometry and the antenna position inside the vacuum chamber.

During the wave launching experiments reported in the next chapter, the plates

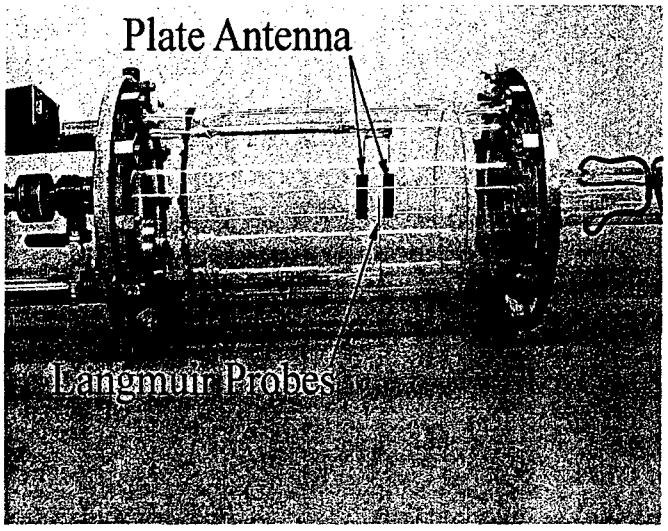

Figure 1.9: Photograph of the BWX test section showing the two-plate ES antenna attached to the moving arm. A set of Langmuir probes attached to the other arm can also can be seen.

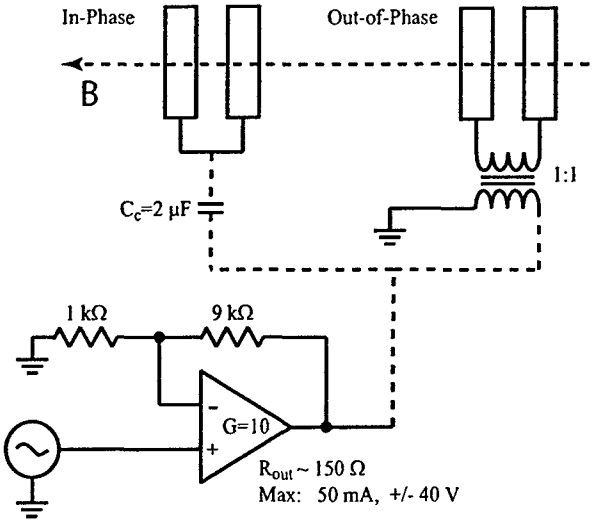

Figure 1.10: Circuit diagram of the two-plate ES antenna, signal generator, and rf amplifier. The two antenna plates can be driven in or out of phase by connecting them to the amplifier through either a capacitor or transformer.

were driven by a single Wavetek 180 signal generator with a sinusoidal signal (10-300 kHz) through a Tektronix AM 501 modular op-amp either in or out of phase, as shown in Fig. 1.10. To increase the power supplied to the ES antenna during the ion heating experiments, the op-amp was replaced by a more powerful broadband ENI 2100L power amplifier with the input and output impedance of 50 Ohm.

1.3.2 Loop ES Antenna

The loop ES antenna, shown in Fig. 1.11, was constructed from four aluminum rings measuring 1 cm wide and 6.7 cm in diameter each. The rings were attached to an arm, similar to that of the two-plate ES antenna, so that the entire antenna assembly could be rotated in and out of plasma, and moved along the axis of the experiment. To prevent ohmic losses each loop was wrapped in Kapton tape. The antenna was inserted into the plasma such that the center axis of all four rings was coincident with the center axis of the experiment and the direction of the magnetic field. The spacing between the center of each loop is 3 cm. Just as with the two-plate ES antenna, the loop spacing controls the parallel wavenumber, $k_{\|}$,while the perpendicular wavenumber, $k_{\perp}$, is free to evolve according to the dispersion relation as a function of wave frequency and other relevant plasma parameters.

While each ring could be supplied with a voltage signal independently, the two useful configurations are $[0, \pi, 0, \pi]$, and $[0, \pi, \pi, 0]$, as described in Ref. [4]. The first configuration establishes parallel wavenumber $k_{\|} = 1$ cm^{-1} ($\lambda \sim 6$ cm), while the second configuration establishes a larger wavelength $k_{\|} = 0.5$ cm^{-1} ($\lambda \sim 12$ cm). In the experiments described in this report the loop ES antenna assembly was driven in the $[0, \pi, 0, \pi]$ configuration. A schematic of the electric circuit used to drive the loop ES antenna is shown in Fig. 1.12. Note that the turns ratio of the transformer in that figure is chosen to optimize the impedance matching between the ENI 2100L amplifier and the antenna.

1.3.3 Beating Waves – Mixing Signals from Two Sources

Beating electrostatic waves can be launched into the plasma by combining the output from two signal sources. This is achieved by mixing the low-power signals from the two Wavetek 180 signal generators and sending the combined output to an amplifier, as shown in Fig. 1.13. The output impedance of the signal generators and the input impedance of the amplifier is 50 Ohms. To make sure that the signal of one of the signal generators is not distorted by the other, the circuit impedance should be matched. A power combiner consisting of a 100 Ohm resistor and a tapped inductor in parallel provide good matching between the signal generators and the amplifier.

1.4 Diagnostics

The BWX diagnostics consist of rf-compensated and uncompensated Langmuir probes and a Laser Induced Fluorescence (LIF) apparatus. The Langmuir probes can be used

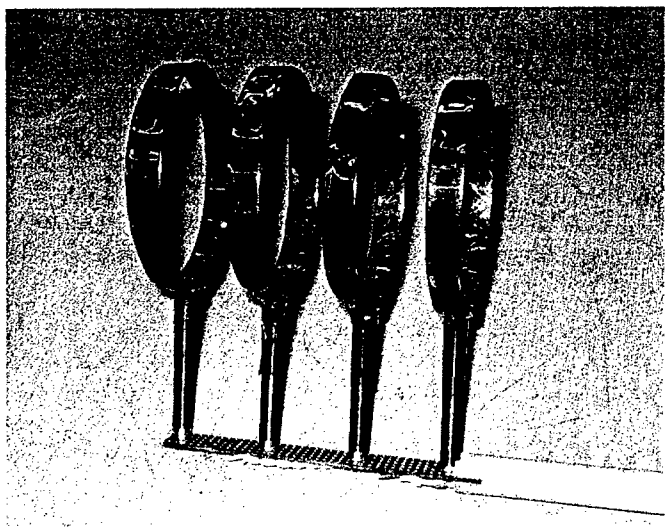

Figure 1.11: Photograph of the loop ES antenna showing its four aluminum rings. The rings are insulated from the plasma by wrapping them in Kapton tape.

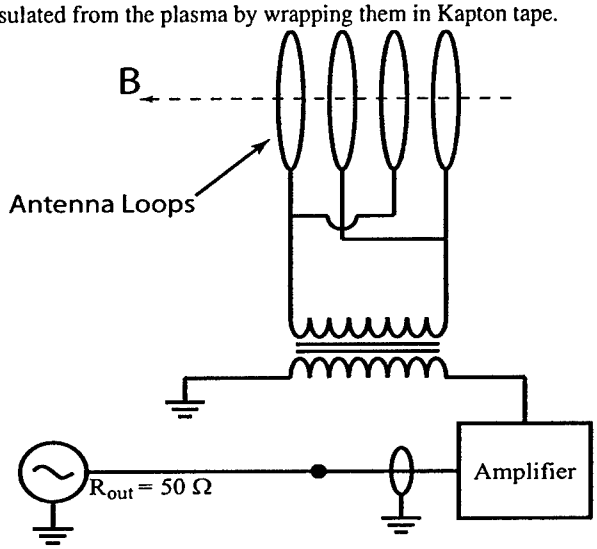

Figure 1.12: Circuit diagram of the loop ES antenna, signal generator, and rf amplifier. The rings are driven by a signal generator through an rf amplifier in either $[0, \pi, 0, \pi]$ (shown here) or $[0, \pi, \pi, 0]$ configuration. The transformer turns ratio is chosen to optimize the impedance matching between the ES antenna and the driving circuit.

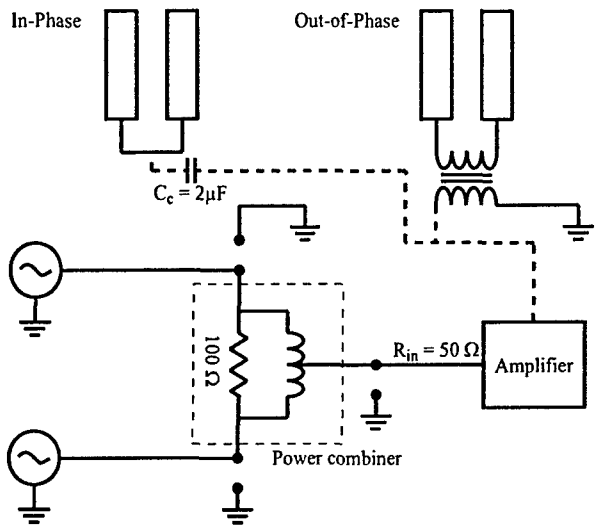

Figure 1.13: Circuit diagram for launching two waves into the plasma column. The impedance between the two signal generators and the amplifier is matched by a power combiner.

to measure the steady-state and pulsed parameters such as the plasma density n_e, electron temperature T_e, as well as to analyze the electrostatic waves dispersion and relative amplitude. The LIF system can measure the perpendicular ion velocity distribution function, and thus yielded the ion temperature. Although this was not done for the experiments reported here, the LIF system could also be reconfigured to measure the parallel ion velocity distribution.

1.4.1 Langmuir Probes

Two types of Langmuir probes were employed to measure the steady-state plasma properties and wave propagation. The plasma density and electron temperature were determined using a radio-frequency-compensated Langmuir probe with 0.5 mm graphite tip [5], shown in Fig. 1.14. The rf compensation was achieved with four miniature inductors placed in series and close to the probe tip. The inductors where chosen to filter out the fundamental (13.56 MHz) and the second harmonic (27.12 MHz) signals of the helicon antenna. The design of the rf-compensated Langmuir probes is described by Sudit and Chen [5].

Instead of the Laframboise analysis [6] of the Langmuir probe I-V characteristic we used the empirical floating potential method developed by Chen *et al.* [7] to determine the T_e and n_e with the rf-compensated Langmuir probes in the rf-sustained plasmas.

A set of three uncompensated Langmuir probes placed orthogonally to each other were also used to measure the perpendicular and parallel wavenumber components of

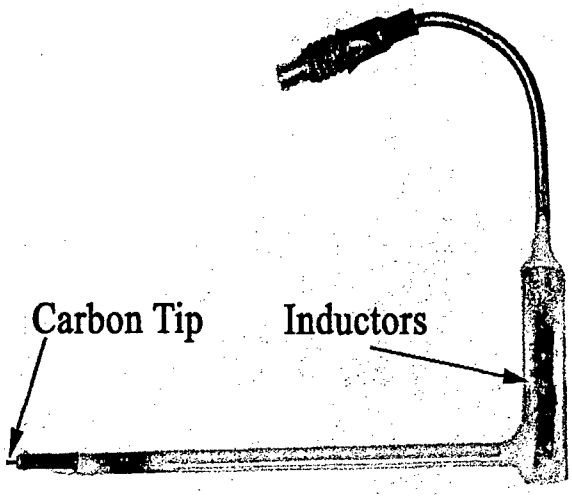

Figure 1.14: Rf-compensated Langmuir probe used to measure the electron temperature plasma density.

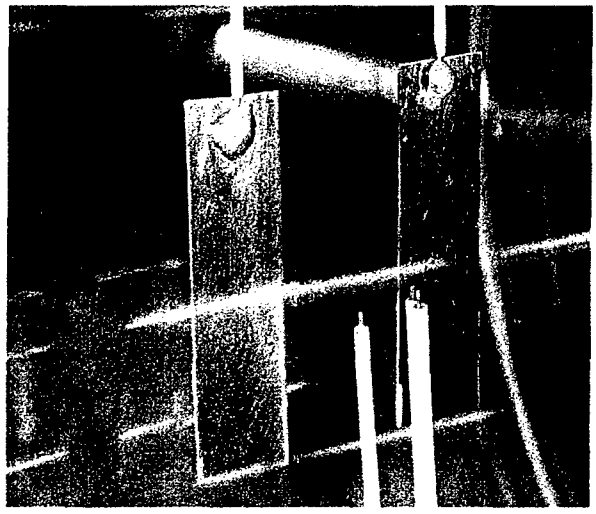

Figure 1.15: Picture of the two-plate antenna together with three Langmuir probes. The three probes can be used to measure the perpendicular and parallel components of the wavenumber as the frequency of the wave is varied.

the propagating electrostatic wave, simultaneously. The three-probe set and its position relative to the two-plate ES antenna is shown in Fig. 1.15. Once the parallel wavenumber was established a system of two probes with T-shaped tips made of 10 mil tungsten wire were used to conduct the further studies. The T shape provided a better signal-to-noise ratio of the Langmuir probe signal.

1.4.2 Electron Temperature and Plasma Density Measurements

A Langmuir probe is the simplest plasma diagnostics device. Typically it is constructed from a thin metal or graphite rod. Langmuir probes can measure electron temperature T_e, plasma density n_e, and electron velocity distribution function $f_e(v)$.

An unbiased probe inserted into a plasma that is at some plasma potential V_p will reach a floating potential V_f. In order to measure the electron temperature and density a sweeping voltage signal is applied to the probe. The amplitude of the voltage sweep is chosen such that the current to the probe oscillates between the ion saturation current I_i^{sat} and the electron saturation current I_e^{sat}. At any point during the sweep the measured current to the probe is $I = I_i - I_e$, where I_i and I_e are the ion and electron contributions to the total current respectively. The electron current becomes negligible when the voltage is swept below the floating potential, and the ion current reaches its saturation limit [7],

$$I_i^{sat} \approx 0.5 q A_p n_e c_s, \tag{1.1}$$

where A_p is the surface area of the probe and $c_s = \sqrt{k_b T_e / m_i}$ is the Bohm velocity. Below the plasma potential, the electron current collected by the probe is exponential,

$$I_e = q n_e A_p v_{te} e^{q(V-V_p)/k_b T_e}, \tag{1.2}$$

where $v_{te} = \sqrt{k_b T_e / 2\pi m_e}$ is the electron thermal speed. The electron temperature can be inferred from the slope of $\ln(I_e)$vs.V plot. Plasma density can subsequently be calculated from Eq. (1.1).

The method outlined above was derived for unmagnetized plasmas [6]. During the experiments described in this report the plasma parameters where such that the ratio of the ion Larmor radius to the Langmuir probe radius is greater than unity, $r_{ci}/r_{probe} > 1$, implying that Eqs. (1.1) and (1.2) can be used.

An improved method of extracting T_e and n_e from the probe's I–V trace was developed by Chen *et al.* [7] specifically for the rf-compensated Langmuir probes in helicon discharges. The method is based on the empirical observation that the ion current has the following power law dependence

$$I_i = V^{3/4} \tag{1.3}$$

The equation above can be fitted to the ion saturation current region, extrapolated to the plasma potential, and then subtracted from the total current measured by the probe. The result is the electron current that can be fitted by Eq. (1.2). This method is explained in more details in Ref. [7]. Figure 1.16 shows a typical I–V trace taken in the BWX apparatus. The figure indicates that both methods give similar results. In that figure

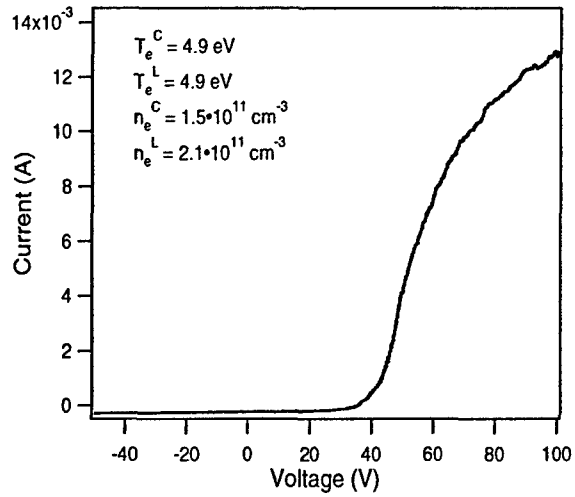

Figure 1.16: Typical I-V trace for the rf-compensated Langmuir probe. Superscript "L" refers to the Laframboise method [6] while superscript "C" refers to the values obtained using the Chen's floating potential method [7].

superscript "L" refers to Laframboise method [6] while superscript "C" refers to the values obtained using Chen's floating potential method [7]. We will adopt Chen's method since it was developed specifically for rf-compensated probes and inductive plasma discharges similar to ours.

1.4.3 Dispersion Relation Measurements

An electrostatic wave is one that has no magnetic field fluctuations. According to Maxwell's equations that leads to a curl-free electric field component,

$$\nabla \times \mathbf{E} = -\frac{1}{c}\frac{\partial \mathbf{B}}{\partial t} \Rightarrow \mathbf{k} \times \mathbf{E} = \omega \mathbf{B} = 0,$$

which means that the wavenumber is aligned along the electric field. Therefore, electrostatic waves are longitudinal in nature. Propagation of an electrostatic wave is characterized by oscillations in the local plasma density. These oscillations can be detected by a Langmuir probe. Thus, Langmuir probes can be used to detect electrostatic waves, analyze their dispersion relation, and measure their electric fields. Two different method involving Langmuir probes can be used to measure the dispersion relation of an electrostatic wave. For this work we used the two-probe method, however a brief description of an interferometric method is also given.

Langmuir Probe Interferometry Method

This technique requires only one Langmuir probe. The interferometric approach relies on comparing the antenna reference signal, $\sin(\omega t)$, with the signal detected by the Langmuir probe, $\sin(kx - \omega t)$, as it is moved relative to the ES antenna. The convolution of the signals, $0.5\{\cos(kx) + \cos(kx - 2\omega t)\}$, contains two spectral components. The wavenumber can be extracted from the graph of the dc component, $\sin(kx)$ vs. x.

The wavenumbers of two or more waves of the same frequency can be separated since the interferometric signal will contain a linear juxtaposition of the sinusoidal terms, $\sin(k_1 x) + \sin(k_2 x) + ...$

The method outlined in this section requires an accurate probe positioning system. In addition, large distances must be traversed by the probe in order to accurately measure waves with long wavelength. Unfortunately, the dimensional constraints of the BWX system make interferometric measurements very difficult.

Two-Probe Method

A simple way to measure the dispersion relation of an electrostatic wave is to compare the phase delay between two or more Langmuir probes separated by a known distance [8]. A plane wave $A\sin(kx - \omega t)$ will introduce a phase delay

$$\Delta\phi = kd \tag{1.4}$$

between the signals from two Langmuir probes separated by a distance d. The component of the wavenumber in the direction of the probe separation can then be found as $k = \Delta\phi/d$. Figure 1.15 shows the three probe system used in the BWX experiment. The system allows simultaneous measurements of $k_{\|}$ and $k_{\perp}$ components.

It is typical for a dispersion relation to have two or more roots for a given wave frequency. Physically this means that two or more waves having different wavenumbers but the same frequency can be sustained by the plasma. In such situation the method described above may produce an erroneous measurement. This can be demonstrated by deriving the phase delay introduced between two Langmuir probes by two such waves, $\sin(k_1 x - \omega t) + \sin(k_2 x - \omega t)$ (assuming the waves have the same amplitude). After some simple algebraic manipulations it can be shown that the phase delay between the signals of the two probes is

$$\Delta\phi = (k_1 + k_2)d/2.$$

It is thus impossible to distinguish between the two waves. However, in our experiments this was not a problems since only one wave was observed. As will be discussed in the next chapter, this wave corresponds to the forward branch of the Electrostatic Ion Cyclotron (EIC) wave. It is possible that a wave corresponding to the backward EIC branch was also excited, but its amplitude was much smaller than that of the forward branch. As can be seen from Fig. 2.3 of the next chapter, the experimentally measured dispersion relation is in good agreement with the forward branch of the EIC wave.

1.4.4 Laser Induced Fluorescence

Various non-invasive spectroscopic plasma diagnostic techniques have been implemented since the development of lasers. One powerful and versatile technique, Laser Induced Fluorescence (LIF), can be used to measure neutral and ion temperatures, flow velocities, plasma density, and even the dispersion relation of electrostatic waves [9, 10].

One of the first measurements of ion velocity distribution and plasma density with a non-tunable LIF system was performed by Stern and Johnson [11]. Development of tunable dye lasers allowed significant improvements and simplifications to the technique [12]. Advances in tunable diode lasers allowed construction of relatively cheap, compact, and portable LIF systems [13].

This section describes the experimental setup consisting of the portable, diode-laser LIF system built as a part of the plasma diagnostics for the BWX experiment. In addition, this section provides a brief overview of the theory behind the LIF ion velocity distribution and temperature measurements.

1.4.5 LIF Theory

The Laser Induced Fluorescence diagnostic technique is based on the Doppler shift of the ion absorbtion lines due to thermal motion and directed drifts. The ion velocity distribution measurement along a particular direction can be achieved by directing a laser beam along that direction. An ion observes the laser frequency ν_l that is Doppler-shifted proportionally to the ion velocity v,

$$\nu_l = \nu_{l0}\left(1 - \frac{v}{c}\right) \qquad \text{for} \qquad \frac{v}{c} \ll 1, \tag{1.5}$$

where c is the speed of light and ν_{l0} is the frequency of the laser signal in the laboratory frame. When the laser wavelength is swept around an ion absorption line, the plot of absorption intensity versus the laser frequency will be proportional to the ion velocity distribution along the direction of the laser beam.

An insightful example of the technique summarized above can be made by assuming the Maxwellian non-drifting ion velocity distribution,

$$f_i(v) \sim e^{-m_i v^2/2k_b T_i}. \tag{1.6}$$

Rearranging Eq. (1.5) and expressing v through $\Delta\nu_l = \nu_l - \nu_{l0}$, the absorption intensity $I_l(\nu_l)$, which is proportional to the velocity distribution, can be written as,

$$I_l(\nu_l) = I_{l0} \exp\left[-\frac{\Delta\nu_l^2}{\nu_{l0}^2}\frac{m_i c^2}{2k_b T_i}\right]. \tag{1.7}$$

Thus, a fit of Eq. (1.7) to the LIF absorbtion intensity data can yield the ion temperature.

1.4.6 LIF Implementation

In practice it is difficult to measure laser light absorbtion. Instead, the laser wavelength is chosen to excite the electrons from a well populated metastable state to some unstable state. The intensity of the emitted light during the transition from the unstable

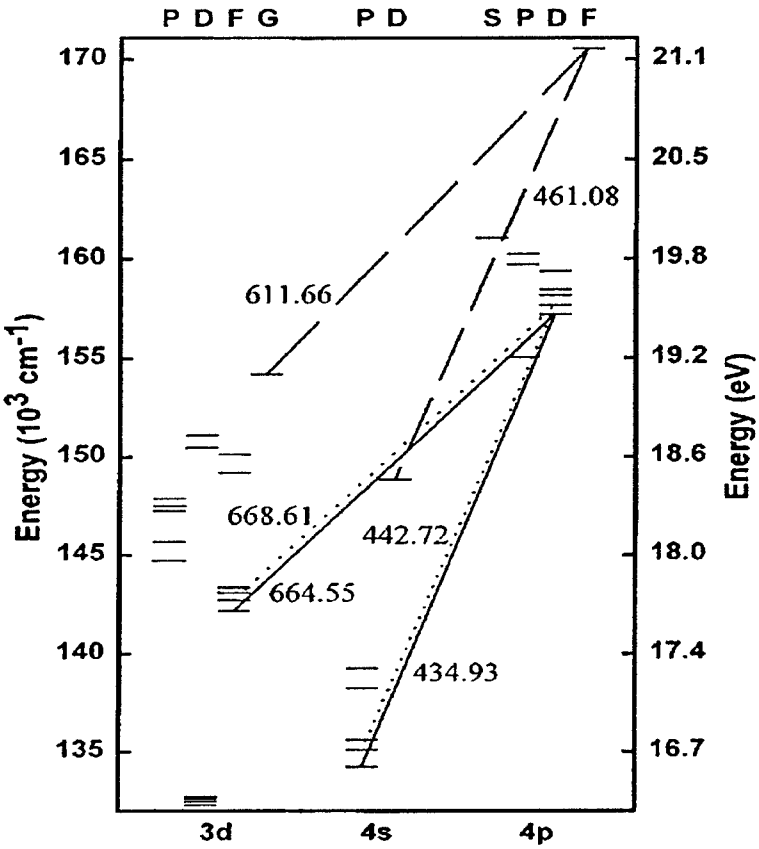

Figure 1.17: Simplified Grotrian diagram for an ArII ion. The diagram shows some possible LIF schemes. The excitation (668.61 nm) and decay (442.72 nm) lines used for the BWX experiments are shown by the dotted lines. The figure is taken from Ref. [13].

state is proportional to the absorbtion intensity, and can be easily measured with a photomultiplier. The photomultiplier signal is then plotted versus the laser wavelength to yield the ion velocity distribution. Some transition lines that can be utilized for the LIF experiments with diode lasers in argon plasmas were investigated in Ref. [13] and are shown in Fig. 1.17. For the BWX experiment a scannable diode laser is tuned to 668.61 nm center wavelength. The chosen wavelength induces the $3d\,^4F_{7/2} - 4p\,^4D^0_{5/2}$ transition in argon ions. The $4p\,^4D^0_{5/2}$ state is unstable and decays quickly to the $4s\,^4P_{3/2}$ state producing 442.72 nm light.

In general, an additional experimental difficulty arises from Zeeman splitting of the transition lines due to the external magnetic field. Other broadening mechanisms, such as natural line broadening, Stark broadening, and power broadening were found to be negligible in similar rf-sustained plasmas [14]. For the perpendicular ion temperature measurements performed during the BWX experiments, the laser was aligned such that the electric field of the light was polarized along the magnetic field. Equation (1.7) can then be used directly to deduce the ion temperature.

1.4.7 LIF Instrumentation

A schematic of the LIF system used for the BWX experiment is shown in Fig. 1.18. A 15 mW Sacher Lasertechnik Lynx tunable diode laser in the Littrow configuration is set to 668.61 nm center wavelength. The laser beam is modulated by a SRS SR-540 chopper spinning at approximately 3.5 kHz. A 10/90 beam splitter allows a Burleigh WA-1500 wavemeter to measure the wavelength of the laser beam with an accuracy of 0.2 ppm. Collection optics focuses the 442.7 nm emission light into an optical fiber which carries the signal to a Hamamatsu HC124-06MOD photomultiplier. A Stanford Research Systems SR830 lock-in amplifier further amplifies the photomultiplier signal with the chopper signal used as a reference. Laser control and data acquisition are achieved with a LabWindows/CVI code written by the WVU helicon source group [15]. For the BWX experiment the code runs on a 950 MHz PC with a National Instruments PCI-6024E and a GPIB data acquisition card through a BNC-2110 connector block and a Tektronix TDS 460A digital oscilloscope.

The LIF system can be used to measure the steady-state as well as time-resolved ion velocity distribution. The steady-state measurements are acquired directly by the computer as the laser wavelength is scanned. For the time-resolved measurements the plasma source needs to be pulsed at a known repetition rate and duty cycle. The plasma source trigger signal, as well as the low integration time signal from the lock-in amplifier, are fed into a TDS 460A oscilloscope. The controlling computer acquires the time-resolved data from the oscilloscope through a GPIB interface.

A picture of the entire LIF assembly is shown in Fig. 1.19. The entire system is small enough to fit on a portable table. The photograph shows all the components except the computer and the oscilloscope.

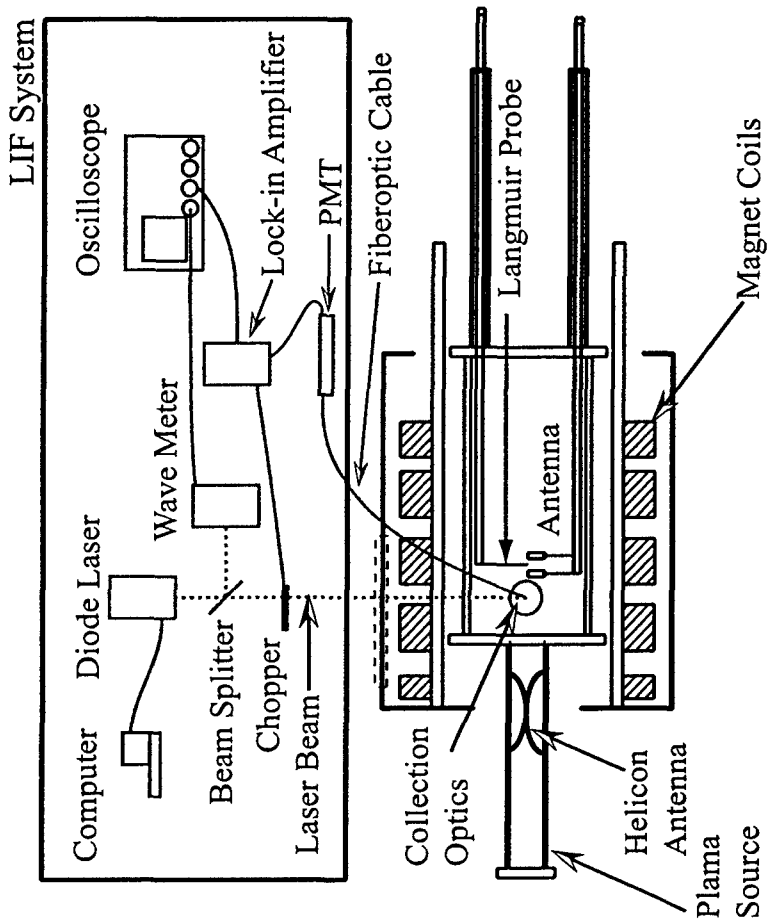

Figure 1.18: Schematic illustrating the LIF setup. The laser wavelength is controlled by a PC through an I/O card. The signal is modulated by a chopper spinning at approximately 3.5 kHz. The signal is detected and amplified by a photomultiplier. The photomultiplier signal is plotted versus the wavelength on a digital scope.

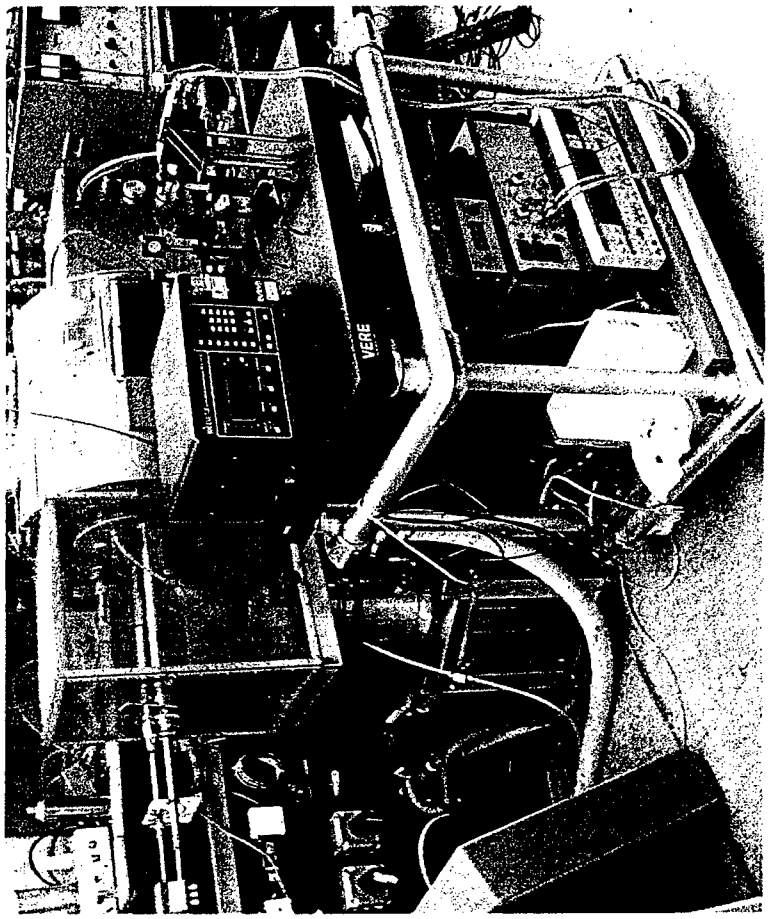

Figure 1.19: Photograph of the portable LIF system in front of the BWX experiment. The picture shows all the LIF components except the computer used to control the laser and the oscilloscope.

1.5 Operation and Procedures

The entire BWX experiment, including the helicon plasma source, can be operated in either steady state or pulsed modes. For pulsed operation, a variable voltage, 100 ms TTL pulses were produced by an HP8116A function generator at 5 Hz and 50% duty cycle. The signal controls the ENI OEM-12A RF power supply, which is used as a power source for the helicon antenna. The same signal can be used as a gate signal for the time-resolved LIF measurements. In addition, the function generator controls a DDG DG565 where the signal can be delayed by an arbitrary amount to trigger the Langmuir probes, ES antenna or other equipment. Most of the experiments were performed with 125 W of rf power to the helicon antenna and only a few watts reflected. The wave launching and time-resolved ion heating experiments were conducted with at least a 30-ms delay from the time the helicon antenna is triggered to ensure that all plasma parameters have reached their steady-state values [16].

Unless stated otherwise, the steady-state LIF measurements were composed of three laser scans. Typical voltage applied to the photomultiplier varied from 600 to 750 volts. For the time-resolved measurements the lock-in integration time was set to 3 ms and each time-resolved wavelength line was averaged over 100 shots.

Chapter 2

Experimental Results and Analysis

In this chapter we present and analyze the data collected during the experimental investigation of the ion heating by beating electrostatic waves. The experiments consisted of two main components. First, dispersion properties of electrostatic waves, which were launched from the two-plate ES antenna into a magnetized plasma column, were characterized. In order to investigate the BEW ion heating mechanism, we needed to ensure that the electrostatic waves propagate in the plasma column at an angle close to 90° relative to the external magnetic field, since we limited the theoretical study that we presented in our previous AFOSR final technical report to propagation perpendicular to magnetic field. Single particle acceleration by oblique beating electrostatic waves has been studied by Strozzi *et al.* [17]. They found that, as long as both beating waves have equal parallel wavenumber, and the angle of propagation is close to 90°, the regular acceleration region remains connected to the stochastic acceleration region, similarly to what was found for the case of perpendicular propagation, which was presented in the final report of the previous AFOSR contract . Measurements of the wave dispersion relation confirmed the electrostatic nature of the waves and determined the angle of their propagation.

The second component of the study involved measurements of the perpendicular ion temperature increase in the presence of the electrostatic waves. Three different measurement techniques were attempted. A Retarding Potential Analyzer (RPA) could not provide a reliable perpendicular ion temperature measurement because the ion Larmor radius in the BWX experiment was on the order of the RPA thickness. Ion temperature can also be inferred from the dispersion properties of the backward branch of the Electrostatic Ion Cyclotron (EIC) wave [18]. However, with the available diagnostics we only observed the forward branch of the EIC wave. We were able to successfully measure the perpendicular ion temperature, using the Laser Induced Fluorescence (LIF) system, described in Chapter 1. Therefore, only the results of the perpendicular ion temperature measurements performed with the LIF technique are reported in this chapter.

In the following section we present and analyze the ES antenna circuit response during the wave-launching experiments. In Section 2.2 we describe the electrostatic wave dispersion and propagation properties in our rf-sustained, magnetized plasma. Effects of ion-neutral collisions on wave propagation are described in Section 2.3. Ion heating by a single and beating electrostatic waves are then compared and contrasted in Section 2.4. Finally, in Section 2.5 we offer some concluding remarks.

2.1 Wave Detection

We conducted the wave dispersion relation studies with the two-plate ES antenna because this antenna coupled better to the plasma than the loop antenna. The waves were detected with a set of uncompensated Langmuir probes with either cylindrical carbon tips or tungsten T-shape tips. A set of three carbon-tipped probes is shown next to the two-plate ES antenna in Fig. 1.15. The circuit used to launch a single electrostatic wave from the two-plate ES antenna into the plasma column is shown in Fig. 1.10. Figure 2.1 shows typical fourier-transformed voltage signals a) driving the ES antenna, b) detected by a Langmuir probe in our plasma, and c) AC coupling between the ES antenna and the Langmuir probe without the plasma. The figure indicates that the AC coupling between the antenna and probe is an order of magnitude below the plasma wave signal, and thus AC coupling does not affect the plasma wave measurements.

To ensure efficient wave generation we needed to maintain good coupling between the ES antenna, its driving circuit, and the plasma. By choosing the appropriate plasma parameters that maximize the amplitude of the launched electrostatic wave for a given input power to the ES antenna we can optimize the coupling. For a fixed magnetic field and neutral pressure, the plasma impedance varies with the plasma density, i.e. with the rf power delivered to the helicon antenna. Therefore, the power delivered to the ES antenna can be correlated with the helicon antenna power.

In order to investigate the wave launching conditions we conducted the following experiment. The signal generator and the op-amp in Fig. 1.10 were set to produce a 30-Volt sinusoidal signal ($f = 60$ kHz). A magnetized argon plasma with $n_e = 10^9 - 10^{13}$ cm^{-3} and $f_{ci} = 30$ kHz was produced by the helicon antenna at various rf powers with the chamber neutral pressure of 1 mTorr. Measuring the ES antenna's voltage and current simultaneously we were able to determine the impedance and power delivered to the antenna plates as a function of the rf power delivered to the helicon antenna. A Langmuir probe inserted into the plasma column measured the amplitude of the launched waves.

As was mentioned in the previous chapter, the plates of the two-plate ES antenna could be driven in or out of phase with each other. We found that for the in-phase configuration the maximum power to the ES antenna plates is delivered when the helicon antenna power is 100-200 W, as shown in Fig. 2.2a. The amplitude of the Langmuir probe signal peaks at ~250 W of rf power, when the real component of the measured impedance (Z_r) approaches 150 Ω, which is the output impedance of the op-amp used in this experiment, and the imaginary part (Z_i) is small. At that condition the entire circuit is closely matched.

A similar experiment was repeated with the antenna plates driven out of phase. The

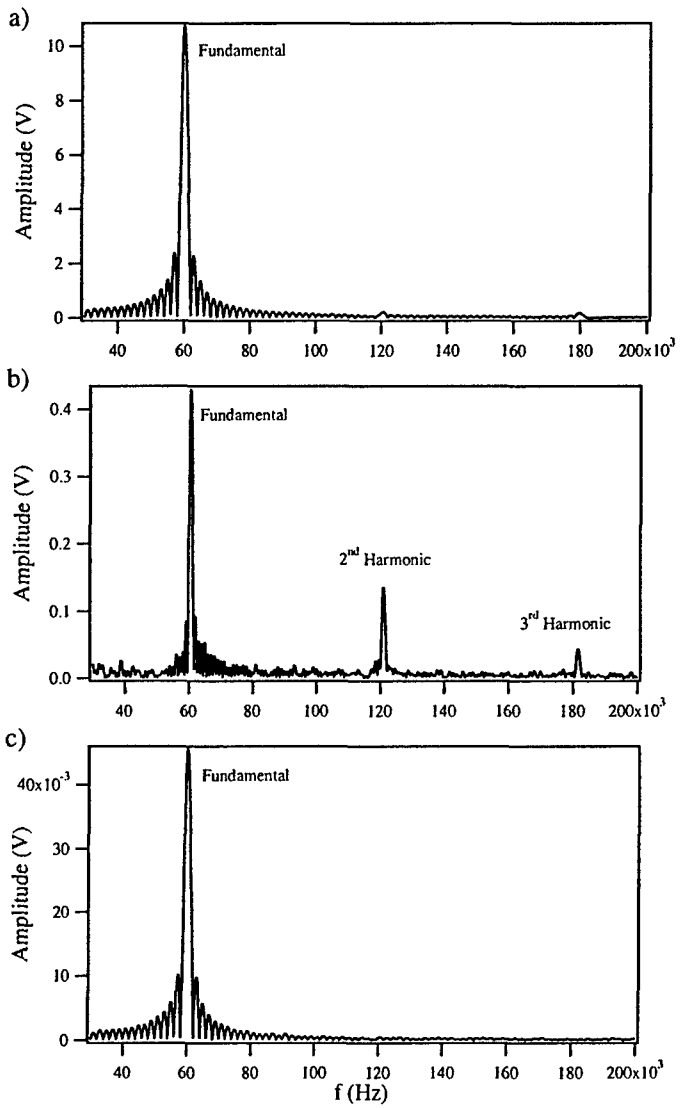

Figure 2.1: Magnitude of the Fourier transform of a typical a) voltage signal to the ES antenna, b) Langmuir probe signal, showing also the second and third harmonics of the excited wave in the plasma, and c) Langmuir probe signal with plasma turned off. The signal is due to the AC coupling between the ES antenna and the Langmuir probe.

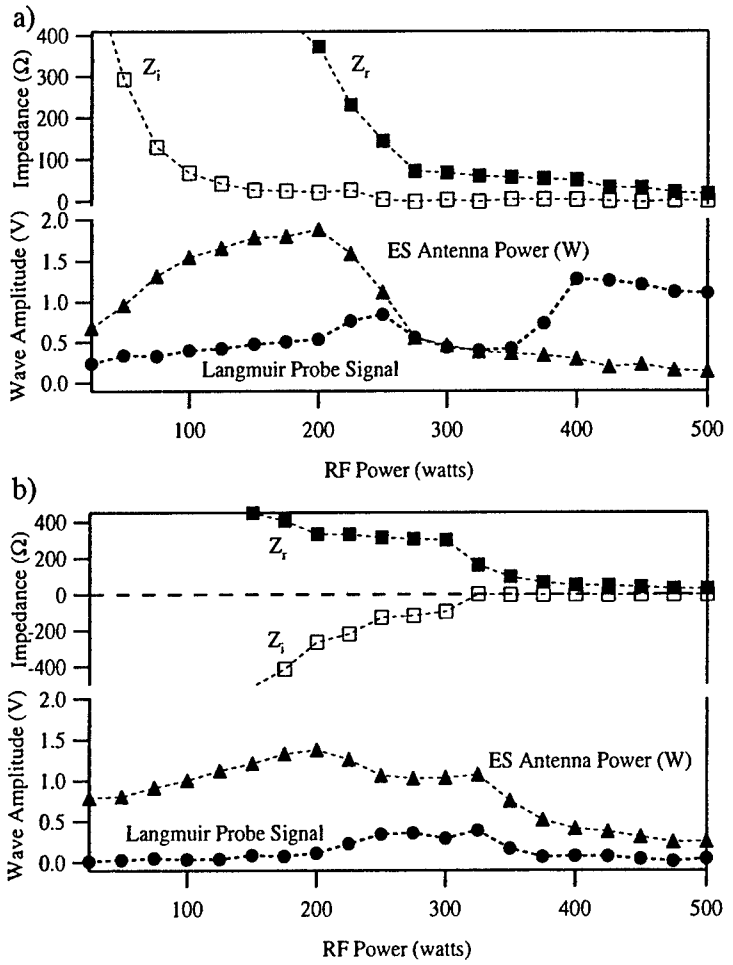

Figure 2.2: The amplitude of the launched ES wave (measured by the Langmuir probe) as well as the impedance and the power delivered to the ES antenna are shown as functions of rf power to the helicon antenna. The real and imaginary components of the ES antenna impedance are designated by Z_r and Z_i respectively. a) Both plates are driven in phase. b) The plates are driven out of phase.

results are shown in Fig. 2.2b. The maximum power in this case is about 75% of that delivered to the ES antenna driven in phase. Also, the wave amplitude detected by the Langmuir probe is significantly lower than the amplitude of the wave launched by the plates driven in phase. Possible reasons for this are given in the next section. However, as in the previous case, the maximum in wave amplitude corresponds to the matched circuit condition, $Z_i \ll Z_r \sim 150\,\Omega$.

The in-phase driven antenna couples better to the plasma, resulting in a wave with a higher amplitude than the out-of-phase driven antenna. We therefore undertook further study of the in-phase configuration. The goal of the study was to determine whether the launched wave is electrostatic in nature and whether it propagates transversely to the magnetic field.

2.2 Dispersion Relation Measurements

Linear electrostatic dispersion relation for a collisional, homogenous, isotropic, non-drifting, and infinite plasma with finite electron and ion temperature, can be derived from the Vlasov equation by including the BGK collision term as described by Choueiri, who performed a similar derivation for unmagnetized ions [19, 20]

$$-i(\omega - k_z v_z - k_\perp v_\perp \cos\theta + i\nu) f_1 + \omega_c \frac{\partial f_1}{\partial \theta} = \frac{iq}{m}\mathbf{k}\Phi \cdot \nabla_v f_0 + \nu \frac{n_1}{n_0} f_0, \qquad (2.1)$$

where f_0, n_0, f_1, and n_1 are the zeroth and first order perpendicular ion velocity distribution functions and particle densities respectively, θ is the angle between the wave propagation and the external magnetic field, and Φ is the electric potential. After some manipulations the first order distribution function can be expressed as

$$f_1 = \frac{q}{T} f_0 \sum_n \sum_m \frac{J_n\left(\frac{k_\perp v_\perp}{\omega_c}\right) J_m\left(\frac{k_\perp v_\perp}{\omega_c}\right) e^{i(n-m)\theta}}{w + i\nu - n\omega_c - k_z v_z} \left[(k_z v_z + n\omega_c)\Phi + i\nu \frac{n_1}{n_0}\frac{T}{q} \right]. \qquad (2.2)$$

The equation above can be integrated over the velocity space to obtain n_1, and then used in Poisson's equation to yield the ES dispersion relation

$$1 + \sum_s \alpha_s \frac{1 + e^{-\mu_s}\xi_{0s} \sum_n I_n(\mu_s) Z(\xi_{ns})}{1 + i(\nu_s/k_z v_{ts}) e^{-\mu_s} \sum_n I_n(\mu_s) Z(\xi_{ns})} = 0, \qquad (2.3)$$

where subscript s refers to the type of the charged species, $\alpha_s = 1/k^2\lambda_{\mathrm{D}s}^2$, $\lambda_{\mathrm{D}s}$ is the Debye length, $\mu = k_\perp^2 v_t^2/2\omega_c$, and $I_n(\mu)$ is the modified Bessel function of the first kind. It could be easily checked that upon setting ν_s to zero, Eq. (2.3) reduces to the familiar collisionless electrostatic dispersion relation, e.g. Eq. (85) given by Stix in Ref. [21]. A more detailed derivation of Eq. (2.3) is given in Appendix A.

To launch an electrostatic ion cyclotron (EIC) wave above the ion cyclotron frequency the following conditions must be satisfied [2],

$$\begin{aligned} \omega_{pi} &> \omega_{ci}, \quad T_i \lesssim T_e, \\ (2T_i/m_i)^{1/2} &\ll \omega/k_\parallel \ll (2T_e/m_e)^{1/2}. \end{aligned}$$

In the reported experiments the following parameters were measured $T_e \sim 3$ eV, $T_i \sim 0.1$ eV, $B = 261$ Gauss, $\omega = 30 - 180$ kHz, and $\lambda_{\|} \approx 46$ cm, and therefore the above inequalities are satisfied. The numerical solution of Eq. (2.3) for the plasma parameters in our experiment is shown in Fig. 2.3. The first panel in that figure shows the solution to Eq. (2.3) in the collisionless limit ($\nu_s = 0$), while the second panel includes the ion-neutral collisional effects (these will be discussed in the next section). In additions, Fig. 2.3b shows the experimentally measured dispersion.

According to Eq. (2.3), two wave modes can propagate in the neighborhood of the ion cyclotron frequency. The first mode is a forward branch of the EIC wave ($\omega/k_\perp$ parallel to $\partial\omega/\partial k_\perp$) with a relatively large wavelength ($\lambda_\perp \sim 6$ cm). The other mode is the backward branch of the EIC wave ($\omega/k_\perp$ antiparallel to $\partial\omega/\partial k_\perp$) with the perpendicular wavelength on the order of the ion Larmor radius. The latter branch is also sometimes referred to as the Neutralized Ion Bernstein Wave (NIBW). In both panels of Fig. 2.3 the forward branch of the EIC and four branches of the NIBW waves are shown by thick lines. The line with the short dashes shows the imaginary part of the perpendicular wavenumber for the forward EIC branch. This wave is weakly damped. On the other hand, the lines with the longer dashes represent the imaginary part of the wavenumber for the NIBW. A large negative imaginary component close to the wave harmonics in Fig. 2.3a indicates that this wave is highly damped at the exact resonances. However, away from the resonance $k_i/k_r \ll 1$ the wave can propagate freely from the ES antenna. Indeed, both the forward and backward branches of the EIC wave have been observed by Skiff *et al.* [1], Alba *et al.* [18], Goree [3], and others in discharges with low neutral density ($\nu_{in}/\omega_{ci} \leqslant 0.02$). As can be seen from Fig. 2.3b, only the forward branch of the EIC wave could be detected in the BWX machine with our diagnostic method.

The dispersion relation for the forward branch of the EIC wave can also be derived from the fluid equations as [22],

$$\omega^2 = \omega_{ci}^2 + v_{ti}^2 k_\perp^2, \tag{2.4}$$

where v_{ti} is the ion thermal speed. As can be seen from this expression, the slope of the forward branch of the EIC dispersion is sensitive to the electron temperature. Thus, comparing the experimentally measured dispersion relation to the theoretical expression provides a good check of the electron temperature. The electron temperature inferred by the slope of the experimental dispersion relation, $T_e = 2.75$ eV, is in good agreement with the values measured independently with the rf-compensated Langmuir probe, shown in Fig. 1.6. Additionally, just as the forward branch of the EIC dispersion relation is sensitive to the electron temperature, the backward is sensitive to the ion temperature [23]. However, since we could not detect the backward branch with our diagnostic methods, the ion temperature in our experiments had to be measured with an alternative method – the LIF.

As was mentioned above, the theoretical dispersion relation given by Eq. (2.3) was derived for an idealized plasma. Some relevant plasma parameters are shown in Fig. 1.8. It can be seen that the plasma is collisional ($\nu_{ei}, \nu_{ii} > f_{ci}$). Also, the density profiles shown in Fig. 1.6 indicate that the plasma is not homogeneous, $(a/n)\partial n/\partial x \gtrsim 1$, specifically at high rf power. Another point of concern is the effect of the plasma boundaries. At low values of $k_\perp$ (long wavelength) the effect of the

boundaries can be significant and the experimental data might diverge from the theoretical prediction. With these considerations in mind, Fig. 2.3b shows a good agreement between the experiments and the theory for a wide range of frequencies.

The experimental dispersion was obtained in the following manner. A single sinusoidal wave was launched by the two-plate ES antenna driven in the in-phase configuration, and inserted at the edge of the plasma column. We measured the wave dispersion by a system of three uncompensated Langmuir probes. The probes were placed orthogonally to each other so that simultaneous determination of $k_\perp$ and $k_\parallel$ could be performed by measuring the signal delay between any two probes [8]. This setup is shown in Fig. 1.15. Measuring the probe signal with the plasma discharge off we determined that the ac-coupling between the ES antenna and the probes was very small (an order of magnitude below the wave signal with the plasma turned on, as shown in Fig. 2.1b and c.

The parallel component of the wavenumber, measured by the two probes placed along the magnetic field, indicated that the parallel wavelength of the wave is 46 cm – the length of the large glass cylinder. The measured perpendicular wavenumber, shown in Fig. 2.3b, varies in accordance with the forward branch of the EIC wave dispersion. The error of the measurements, shown by a horizontal bar in the lower right corner of the figure, was calculated from multiple (10–30) measurements at the same conditions. The dispersion measurements at frequencies up to $\omega/\omega_{ci} = 10$ indicate that the wave propagates at the angles of 82° to 86° with respect to the magnetic field. It should be noted that, while theoretical work presented in the final report of the previous AFOSR contract strictly applies only to the perpendicular wave propagation, recent theoretical work by Strozzi *et al.* [17] shows that we should expect the BEW heating mechanism to exist even when the waves propagate obliquely with respect to the magnetic field, as long as the waves have the same wavenumber. This is indeed the case in our experiment since both beating waves were launched from the same antenna simultaneously. For both waves, the parallel wavenumber was established either by the plate spacing or the physical dimensions of the chamber.

We should also note that when the antenna plates were driven out of phase, the measured dispersion relation did not follow the theoretical dispersion relation for the EIC wave. According to the previous discussion, we expected the parallel wavelength for the out-of-phase configuration to be 6.28 cm – twice the spacing between the plates. However, the measured parallel wavelength was on the order of the chamber length, similar to the in-phase configuration. While we have not investigated this in detail, it is possible that the wave propagation was affected by the closeness of the conducting end-plates of the vacuum chamber or by ion Landau damping since, for that configuration, $w/k_\parallel \sim v_{ti}$. For the experiments presented in the following sections we, therefore, used only the in-phase configuration.

2.3 Effects of Ion-Neutral Collisions

As we have discussed earlier, the effects of ion-neutral collisions can be investigated by including the BGK collisional operator into the Vlasov equation. For argon, at temperatures and densities typical to the BWX experiment, the charge-exchange and

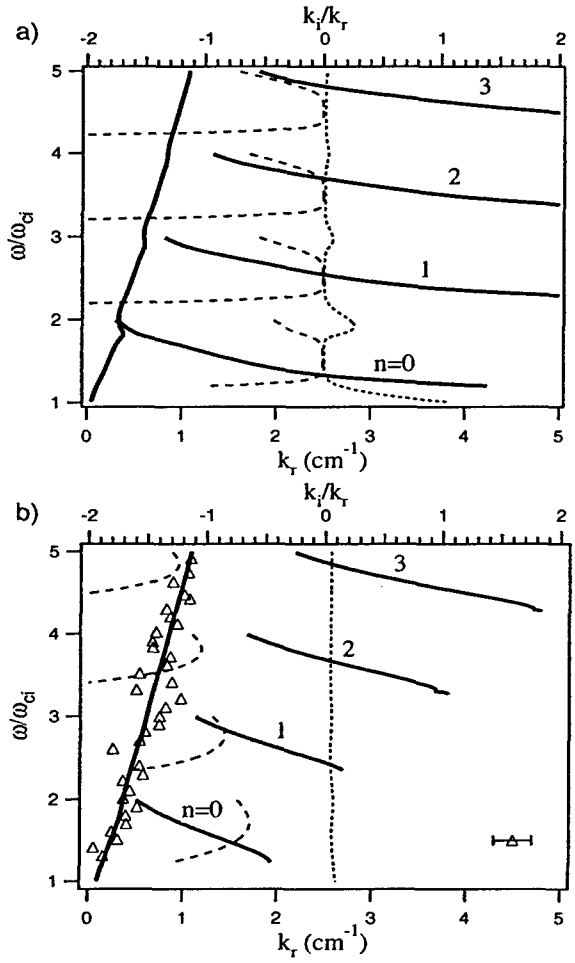

Figure 2.3: Electrostatic dispersion relation for the waves propagating in an argon plasma slightly above the ion cyclotron frequency obtained from Eq. (2.3) for a) collisionless plasma, b) a plasma typical to the BWX experiment, including ion-neutral collisions at 1 mtorr. The thick black lines show the wave frequency as a function of the real component of the wavenumber, while the dashed lines show the wave frequency as a function of the imaginary component of the wavenumber (top scale). Experimentally measured dispersion relation (Δ) is also shown. Other plasma parameters common to both a) and b) are B=261 G, T_e=3 eV, $T_{i\perp}$=0.11, and $k_{\|}$=0.14 cm^{-1}.

ion-neutral elastic scattering collision cross-sections are on the order of $\sim 10^{-14}$ cm^2 [24, 25], and the total ion-neutral collision frequency can be estimated to be $\sim 1.5\times10^4$ s^{-1}. Therefore, in our experiment $\nu_{in}/\omega_{ci} = 0.2$, which is an order of magnitude higher than in Skiff's experiment [1]. Even though the ratio of ion-neutral collisions to the ion cyclotron frequency is small ($\nu_{in}/\omega_{ci} < 1$), we now show that the collisions nevertheless significantly alter the EIC wave propagation.

When ion-neutral collisions are taken into account in the dispersion relation, the backward branch of the EIC wave becomes highly damped at all frequencies. Figure 2.3b shows solutions to Eq. (2.3) that include ion-neutral collisions. Note that collisions have little effect on the real part of the forward branch of the dispersion relation. While the forward branch of the EIC wave is mainly unaffected, the imaginary part of the NIBW wavenumber grows significantly. For example, with $\omega/\omega_{ci} = 1.5$ the imaginary part of the wavenumber, k_i, increases by three orders of magnitude to $k_i \sim k_r$ (k_r is the real part of the wavenumber), as compared to the collisionless case. Thus, for our collisional plasma we expect the backward branch of the EIC wave to be damped within a short distance away from the ES antenna. As was mentioned above, we did not observe the backward branch of the EIC wave. However, the experimental dispersion relation, shown in Fig. 2.3(b) by triangles, is in a good agreement with the solutions to Eq. (2.3) for the forward branch of the EIC wave.

For the conditions of our experiments, with the plate antenna driven in phase, we were able to launch the forward branch of EIC, which despite the attenuating effect of ion-neutral collisions propagates in the vicinity of the antenna. While we were only able to measure the dispersion relation of the forward branch, it is possible that the heating reported in the next section could be due to the backward branch, whose amplitude may have been too small to detect by our diagnostic, because it is known to have better coupling with the ions.

2.4 Ion Heating in the BWX

The NIBW mode interacts with ions much stronger than the forward branch of the EIC wave, because its wavelength is on the order of the ion Larmor radius. Therefore, to observe any significant ion heating by an electrostatic wave in a warm, dense discharge, either the amount of power to the ES antenna or the magnetic field should be increased. The former increases the amount of power transferred from the waves to the ions. The latter decreases the ratio ν_{in}/ω_{ci}, thus making the plasma less collisional, allowing the NIBW to propagate. The magnetic field in the BWX experiment is limited by the amount of the current available from the magnet power supply. To reduce ν_{in}/ω_{ci} to an acceptable level in our experiment, the magnetic field should be increased to at least 0.3 T, which is three times the amount available. Therefore, we have chosen the route of increasing the power by amplifying the signal to the ES antenna. We have observed ion heating with the two-plate and the loop ES antennas. The heating with the two-plate ES antenna was more pronounced than heating with the loop ES antenna because more power could be transferred to the plasma from the former than the latter.

We first performed a time-resolved study of ion heating by a single electrostatic wave launched by the two-plate ES antenna. For this study, all plasma parameters were

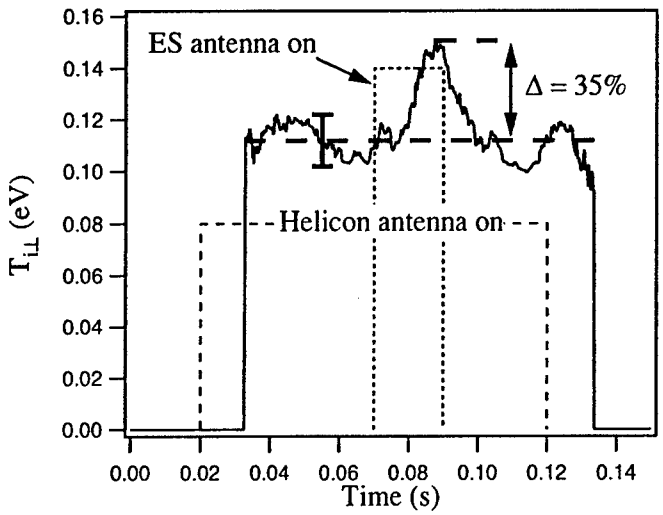

Figure 2.4: Ion temperature evolution for a 100 ms plasma pulse. A steady-state plasma is established 15 ms after the rf power is applied to the helicon antenna. Perpendicular ion temperature increases by ~35% when an electrostatic wave propagates from the two-plate ES antenna. When the two-plate ES antenna is turned off the ion temperature returns to its ambient level.

similar to the experiments described in Refs. [15] and [26]. The plasma was created by sending a 100 ms, 125 W rf pulse to the helicon antenna. The two-plate ES antenna was turned on for 20 ms with a delay of 50 ms (to ensure that the plasma has reached a steady state), as shown in Fig. 2.4 by the dashed boxes. For the first 15 ms after the helicon antenna was turned on we observed a population of fast ions propagating through the plasma column. The velocity distribution of this population was found not to be Maxwellian, and thus a perpendicular ion temperature could not be established. The plasma reached a steady state after about 15 ms with an average temperature of 0.11 eV, shown by the thick dashed horizonal line in Fig. 2.4. The uncertainty in the temperature measurement can be determined from the temperature fluctuation when the two-plate ES antenna is off. Analysis shows that this error, shown by the vertical bar in Fig. 2.4, is $\sim$0.01 eV or 10%. We have also confirmed this uncertainty through a series of repeated steady-state ion temperature measurements with the two-plate ES antenna turned off.

When the ES antenna was turned on, we observed significant rise in the ion temperature. Figure 2.4 shows a 35% temperature increase. However, this increase is an order of magnitude below that reported by Skiff *et al.* [1] in a less collisional plasma of a Linear Magnetized Device, but on the same order as reported by Kline *et al.* [27, 28] in an rf-sustained plasma. This is not surprising since we expect ion-neutral collisions to play an important role in damping the waves.

Ion heating was observed within only a short distance from the two-plate ES antenna. While the position of the antenna relative to the LIF measurement volume could not be precisely controlled, we observed a sharp increase in the ion temperature as the ES antenna was moved within half a centimeter of the LIF laser beam. This observation qualitatively supports prediction of the collisional dispersion relation in Fig. 2.3b.

Next, we performed a study of the beating wave ion heating in a steady-state plasma. Time-resolved measurements are quite time consuming; it takes about 30 minutes to obtain a time-resolved ion temperature profile with 31 different laser wavelengths. A small drift in the helicon antenna tuning may change plasma parameters over this period. This renders the time-resolved measurements impractical for comparison between different scans. On the other hand, a measurement of a steady-state plasma with 300 different wavelengths can be performed under 30 seconds. For this experiment we have compared ion heating by a single electrostatic wave with $\omega = 3.5\omega_{ci}$ to that resulting from two beating waves with $\omega_1 = 3.5\omega_{ci}$ and $\omega_2 = 4.5\omega_{ci}$. To ensure that the comparison is valid we set the total power for both beating waves to be the same as that for the single wave. Figure 2.5 shows the results of these experiments as a function of power delivered to the ES antenna. Each data point is an average of three measurements.

Experiments revealed a threshold in the ES antenna power (wave amplitude) at about 2 W, above which there is a significant ion heating for both single and beating waves, as shown in Fig. 2.5. Power to the ES antenna was calculated by the simultaneous measurements of the oscillating current and voltage delivered by the amplifier. When the ES antenna power was below 2 W we did not observe ion heating with either single or beating electrostatic waves. As the antenna power was increased above 2 W, ion temperature also increased for both SEW and BEW heating mechanisms. This behavior can be explained with the help of the wave-amplitude threshold (not to be

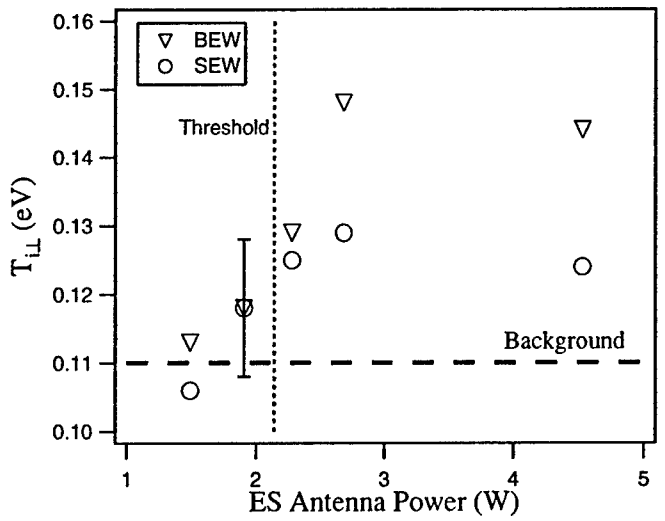

Figure 2.5: Results of the BEW (▽) and SEW (o) ion heating experiments. The background perpendicular ion temperature is 0.11 eV, and is shown by the thick dashed line. The plot shows a heating threshold in wave power (amplitude) at about 2 W above which there is significant heating for both BEW and SEW schemes. The data also indicates a threshold at about 2.5 W above which the perpendicular ion temperature is higher for the BEW heating scheme.

confused with the velocity threshold) derived from the single-particle model developed by Karney [29]:

$$E/B = \frac{1}{4}(\omega_{ci}/\omega)^{1/3}(\omega/k_\perp). \tag{2.5}$$

Using this equation we can determine the electric field amplitude of the wave at the threshold. Then, from Fig. 2.2a we can estimate the minimum ES antenna power needed to observe the ion heating. For the parameters of our experiments, the amplitude of the electric field at the threshold determined by Eq. (2.5) is 0.14 V/cm. With the wavenumber of 0.7 cm^{-1} (from Fig. 2.3 at $\nu = 3.5$) this corresponds to 0.6 V of the probe signal. Figure 2.2a shows that, at 125 W of RF power, and with $\sim$ 1.5 W of power into the ES antenna, the Langmuir probe signal is 0.42 V. A simple extrapolation of that signal to 0.6 V gives 2.14 W needed at threshold. This threshold is shown in Fig. 2.5 by a vertical dashed line, and is in good agreement with the power above which ion heating is observed shown in 2.5. Similar threshold behavior was observed by Skiff *et al.* [1], who investigated ion heating by SEW in a less collisional plasma. At ES antenna powers below this threshold we do not observe significant ion heating, while at powers above this threshold ions are heating by both SEW and BEW mechanisms.

In previous chapters we have shown that the BEW heating mechanism has the potential of providing a more effective method of ion heating than the SEW mechanism because beating electrostatic waves can interact with ions below the single-wave velocity threshold, given by Eq. (1.4) (quoted below) of the report from the previous AFOSR contract . We expect that a wave interacting with a larger number of ions will be able to produce higher ion temperatures. Figure 2.5 shows that as the ES antenna power level is increased above 2 W, the ion temperature resulting from the BEW heating increases over that of the SEW heating. To ensure that the increase in the heating effectiveness of the BEW mechanism is due to the waves interacting with particles whose initial velocity is below the SEW velocity threshold, we check that the bulk of the initial ion velocity distribution function falls below the threshold given by Eq. (1.4) of the report from the previous AFOSR contract, which we quote here for convenience

$$v = \frac{\omega}{k_\perp} - \sqrt{\frac{qE}{k_\perp m_i}}. \tag{2.6}$$

Using the value of electric field calculated above, we find that the threshold velocity is $\sim 3 \times 10^5$ cm/s, which is higher than the ion thermal velocity, $v_{ti} \sim 5 \times 10^4$. We, therefore, conclude that the bulk of the initial ion velocity distribution function is below the single-wave velocity threshold for the SEW and BEW, and the higher ion temperature observed with the BEW is a manifestation of threshold-less behavior that allows a larger portion of the distribution function to be energized. We found that the BEW ion heating is $\sim$15% stronger than the SEW heating for the particular conditions used in this experiment. This provides the first evidence of an increase in efficiency between SEW and BEW heating. We expect that this enhancement would be much more significant without the effects of collisions.

The loop ES antenna could not be coupled to the plasma as well as the two-plate antenna. As the result, the heating produced by the loop antenna was significantly

smaller. Using the loop antenna, we have attempted to heat ions with either a single or beating waves at frequencies varying from 30 kHz up to 1.8 MHz. We were able to heat ions by ~15% with a wave at 450 kHz, and by ~2.4% at 1.8 MHz. It is interesting to note that at the latter frequency the ion heating most likely results indirectly from the interaction between the lower-hybrid waves and the electrons. Nevertheless, beating waves with $\omega_1 = 1.77$ MHz and $\omega_2 = 1.8$ MHz produced ~5% heating, which is twice the heating produced by the single wave at 1.8 MHz.

2.5 Final Remarks

In this chapter we have reported on the excitation and propagation of Electrostatic Ion Cyclotron (EIC) waves launched by the two-plate ES antenna into a magnetized, rf-sustained argon plasma. We described in detail the circuity necessary to drive the ES antenna in the in- and out-of-phase configuration. We found that the ES antenna driven in phase couples better to the plasma and can excite a higher amplitude wave than the plates driven out of phase. In addition, we determined that the wave amplitude can be optimized by carefully choosing the right plasma parameters and selecting appropriate electric components to match the driving circuit.

The ES antenna driven in phase excited a wave with $\lambda_{\parallel} = 46$ cm - the length of the test section of the vacuum chamber. The perpendicular component of the wavenumber varies according to the EIC dispersion relation, and is in good agreement with the forward branch of the theoretical dispersion relation despite the simplifying assumption of a homogeneous, isotropic, and infinite plasma slab. As a part of the study we have also investigated the effects of ion-neutral collisions using the electrostatic dispersion relation, and shown that the backward branch of the EIC wave is strongly damped by these collisions. We found that the forward branch of the EIC waves launched at frequencies between ω_{ci} and $10\omega_{ci}$ can propagate with little damping at an angle between 82° and 86° with respect to the magnetic field.

We have also reported on an experimental investigation of the ion heating by a single and beating electrostatic waves in order to explore the heating enhancement predicted by the theory of ion acceleration by beating electrostatic waves. We were able to produce ion heating with a single and beating waves using two different ES antennas. Using the two-plate antenna we were able to increase the ion temperature by ~35% above background. We observed a threshold behavior consistent with the single-particle theory for both single and beating wave heating by increasing the power to the ES antenna. In addition, we showed that beating waves can consistently heat ions to higher temperature than a single wave within the error bar of the measurement. This enhancement in ion temperature was found to be 15% for the particular conditions of these experiments, but is expected to be significantly higher in a less collisional plasma. This observation supports the theoretical prediction that beating electrostatic waves interact with ions moving below the single-wave velocity threshold.

Chapter 3

Conclusions

This report presented the work done under AFOSR contract FA9550-05-1-0181, which is a 1-year continuation of contract F49620-02-1-0009. The project is an investigation of the ion heating by beating electrostatic waves (BEW) in a magnetized plasma. This type of heating mechanism may be promising for various applications because the BEW interaction is inherently a non-resonant process that allows the waves to energize arbitrarily slow particles.

Previous works on the BEW heating mechanism [30, 31] were limited to theoretical investigations dealing with one magnetized charged particle. In addition, the theory lacked a description of the necessary and sufficient conditions that govern this interaction. Furthermore, effects of collisions on this interaction have not been investigated. Finally, no experimental studies of the stochastic ion heating by beating electrostatic waves have been previously reported. The work presented in this report has thus been channeled along three directions: 1) theoretical, 2) numerical, and 3) experimental with the following specific aims

- To improve the single-particle theory of the BEW ion heating. Specifically, to determine the necessary and sufficient conditions for the stochastic wave-particle interaction to occur.
- To understand the applicability of the BEW ion heating mechanism to warm collisional plasmas.
- To perform an experimental demonstration of the BEW heating for the first time in a laboratory environment.

3.1 Summary of Major Findings

3.1.1 Theoretical Findings

Theoretical investigation (presented in the final report of the previous AFOSR contract) of the model describing the stochastic interaction between a single charged and

magnetized particle and beating electrostatic waves revealed that the beating criterion

$$\omega_1 - \omega_2 = n\omega_c,$$

described by Benisti *et al.* [30, 31] provides the necessary but not sufficient condition for the stochastic interaction to occur.

We have found that the necessary and sufficient conditions can be described through the positions of the elliptic and hyperbolic points in the regular acceleration region on the Poincaré section describing the BEW acceleration. These points define an energy well that a particle must overcome in order to be stochastically accelerated by the beating waves. In the notation used throughout this report we call this well the forbidden acceleration region of phase space. This forbidden region can be described by the Hamiltonian of the two critical points.

$$\begin{aligned} H([\nu - \sqrt{\varepsilon}]/2; \pi) &< H(\rho_0; \vartheta_0) < H(\nu - \sqrt{\varepsilon}; \pi), \\ \text{with } \rho_0 &< \nu - \sqrt{\varepsilon}, \end{aligned} \tag{3.1}$$

where the subscript "0" refers to the particle initial position on the Poincaré section (i.e. its velocity and phase angle), and H is the system Hamiltonian. Equation (3.1) states that a particle with the Hamiltonian inside the energy well does not interact with the beating waves strongly, and its energy oscillates between the high and low points of the well. On the other hand, particles outside the well are said to be in the allowed acceleration region. These particles strongly interact with the waves, and on average gain energy.

3.1.2 Numerical Findings

While useful, the theoretical model is limited to the BEW interaction with a single particle. In a real plasma, other processes, such as collisions between ions, electrons, and neutral atoms can alter the heating mechanism. We have studied the effects of ion-ion collisions on the BEW heating scheme by conducting Monte Carlo simulations.

Our simulations have shown that ion-ion collisions improve the heating effectiveness of the BEW as well as SEW schemes. In a real plasma, initial ion temperature, plasma density, and wave frequencies can be chosen to optimize the effectiveness of the BEW heating mechanism over that of the SEW.

We have also found that for collisionless plasmas the maximal energy attained by the simulated system (i.e. its temperature, when the distribution is Maxwellian) is a complex function of the wave frequency. Using an analytical model that is based on a simple physical argument we were able to predict the maximal energy dependence on the wave frequency. This model may serve to optimize the plasma and wave parameters for future detailed experimental investigations of the BEW heating mechanism.

3.1.3 Experimental Findings

We have found that an EIC wave could be launched into a magnetized, rf-sustained plasma from a two-plate ES antenna at frequencies up to $10\omega_{ci}$. These waves propagate

at the angles between 82° and 86° relative to the external magnetic field. According to the single-particle theory these waves can result in significant ion acceleration [17].

We have also found that in a warm, collisional plasma that is sustained by an rf source, ion-neutral collisions play a key role in electrostatic wave propagation. This effect was not considered in the theoretical and numerical investigations that we have conducted because these studies focused on the wave-particle interaction, and not on the wave generation and propagation mechanisms. For an ion-neutral collision frequency of $\sim 0.2\omega_{ci}$ we found that the backward branch of the EIC wave is strongly damped. Since this is the branch mostly responsible for the wave-ion interaction, the BEW heating mechanism, for our particular experiment, was strongly affected by ion-neutral collisions.

Nevertheless, we have found that even in such a collisional plasma, ions can be heated by $\sim$ 35% over background level by the electrostatic waves. We have confirmed a threshold in wave energy above which we observe ion heating for both the BEW and SEW mechanisms. This threshold was predicted theoretically by Karney *et al.* [32, 29, 33] and confirmed experimentally by Skiff *et al.* [1] for the single wave heating. Furthermore, we have found that the BEW interaction resulted in 15% greater temperature increase than the SEW interaction (at the same overall wave energy). Based on the dependencies discussed in Chapter 2 of the report from the previous AFOSR contract, we expect the BEW mechanism to result in significantly higher heating in a less collisional plasma, where the relevant parameters are optimized to enhance the heating.

3.2 Recommendations for Future Work

The theoretical, numerical, and experimental studies reported in this report, and the one from the previous contract, constitute an early step in the exploration of the BEW heating mechanism. Now that the basics of the mechanism have been elucidated, a more detailed study should be conducted to investigate the relevance of this mechanism to plasmas used specifically for space propulsion applications.

One avenue for investigation can include a more detailed numerical study that simulates the effects of collisions between all species, and includes geometric factors, such as the ES antenna extent, chamber dimensions, and plasma flow past the antenna. This will most likely require an involved PIC/DSMC solver that was beyond the scope of the goals set for the project.

Another direction for future work can be focused on improving the experimental parameters to yield higher ion heating. As we have found, a key parameter for the wave propagation in our experiment is the ratio of ion-neutral collision frequency to the ion cyclotron frequency. This ratio should be lowered at least an order of magnitude in order to observe significant stochastic ion heating. There are multiple ways of achieving this goal. For example this could be done either by increasing the ion cyclotron frequency or lowering the ion-neutral collision frequency.

Lowering ion-neutral collision frequency significantly may require a different plasma source, since rf sources cannot maintain discharges at a neutral pressure much lower than used in the BWX experiment. A good candidate is a Q-machine that can sustain

high plasma density while maintaining very low neutral pressure.

On the other hand, the ion cyclotron frequency can be raised by either increasing the magnetic field or utilizing a lighter gas. Both solutions are feasible, but come with their own set of problems. Increasing the magnetic field requires an expensive magnet power supply, and a magnet capable of conducting high currents without overheating. One possible solution to overheating is to pulse the magnet.

Using a lighter gas may make it hard to measure the ion temperature. For example, helium atom is ten times lighter than argon, and may be an ideal candidate for future experiments. However, direct measurements of the helium ion temperature with LIF appears to be quite difficult [34]. As described in Chapter 2, temperature measurements with RPA and using the ES wave interferometry have also proven unsuccessful in the BWX experiment. An indirect measurement may still be possible.

Finally, ion-neutral collision frequency can be lowered by an appropriate choice of initial conditions, such as ion temperature and plasma density, as well as judiciously selecting ES wave frequency, as discussed Chapter 2 of the final report from the previous AFOSR contract. While decreasing the plasma density while maintaining the same ionization fraction is difficult to achieve in rf-sustained plasma devices, ion temperature could be raised with various means. If the ion temperature is increased by an order of magnitude, significant BEW ion heating with the lower-hybrid waves should be expected as predicted by the numerical simulations presented in Chapter 2 of the final report from the previous AFOSR contract.

Appendix A

ES Dispersion for a Homogeneous, Isotropic, Magnetized, Collisional Plasma

Physics is like sex. Sure, it may give some practical results, but that's not why we do it. – Richard Feynman

In this appendix we derive the electrostatic dispersion relation for a homogeneous, isotropic, magnetized, collisional plasma. A very similar derivation was made by Choueiri [19] for umagnetized ions. Here we generalize that derivation to include magnetized ions. We also model the ion-neutral collisions through an adjusted BGK collision operator as described by Dougherty in Ref. [35]. The first-order Vlasov equation for any charged species can be written as

$$\frac{\partial f_1}{\partial t} + \mathbf{v} \cdot \nabla_x f_1 + \frac{q}{m} E_1 \cdot \nabla_v f_0 + \frac{q}{m} \mathbf{v} \times B_0 \cdot \nabla_v f_1 = -\nu \left(f_1 - \frac{n_1}{n_0} f_0 \right), \quad \text{(A.1)}$$

where all first-order variables vary as $e^{i(k \cdot v - \omega t)}$, and ν is the collision frequency. Note that by summing over all charged species the final dispersion relation will be general enough to include all collisions in a plasma (i.e. ion-neutral and electron-neutral collisions). The following operator substitutions can now be made: $\partial/\partial t \rightarrow -i\omega$ and $\nabla_x \rightarrow i\mathbf{k}$. The equation above can be rewritten as,

$$-i(\omega - k_z v_z - k_\perp v_\perp \cos\theta + i\nu) f_1 + \omega_c \frac{\partial f_1}{\partial \theta} = \frac{iq}{m} \mathbf{k}\Phi \cdot \nabla_v f_0 + \nu \frac{n_1}{n_0} f_0, \quad \text{(A.2)}$$

where we have expressed the electric field of the wave as $E_1 = -i\mathbf{k}\Phi$ and switched to cylindrical coordinates, shown in Fig. 2.1 of the final report from the previous AFOSR contract. We have also assumed, without any loss of generality that $\mathbf{k} = k_\perp \hat{y} + k_z \hat{z}$. After dividing by ω_c we see that the equation above is a first-order, ordinary, inhomogeneous equation of the type $y' + P(x)y = Q(x)$, which can be solved by the method

of integrating factors [36] to obtain the following solution,

$$\begin{aligned} f_1 &= \frac{1}{\omega_c}\left[\frac{iq}{m}\mathbf{k}\Phi\cdot\nabla_v f_0 + \nu\frac{n_1}{n_0}f_0\right]e^{\frac{i(w+i\nu-k_z v_z)}{\omega_c}\theta}e^{-i\frac{k_\perp v_\perp}{\omega_c}\sin\theta} \\ &\times \int e^{\frac{i(w+i\nu-k_z v_z)}{\omega_c}\theta}e^{i\frac{k_\perp v_\perp}{\omega_c}\sin\theta}d\theta. \end{aligned} \tag{A.3}$$

With the help of the following identities

$$f_0 = \frac{n_0}{\pi\sqrt{\pi}v_t^3}e^{-v_\perp^2/v_t^2}e^{-v_z^2/v_t^2}, \tag{A.4}$$

$$e^{i\frac{k_\perp v_\perp}{\omega_c}\sin\theta} = \sum e^{in\theta}J_n\left(\frac{k_\perp v_\perp}{\omega_c}\right), \tag{A.5}$$

$$e^{-i\frac{k_\perp v_\perp}{\omega_c}\sin\theta} = \sum e^{-in\theta}J_n\left(\frac{k_\perp v_\perp}{\omega_c}\right), \tag{A.6}$$

$$\sum J_n(z) = \sum \frac{n}{z}J_n(z), \tag{A.7}$$

where J_n is the Bessel function of the first kind and v_t is the species thermal velocity, the first-order velocity distribution can finally be rewritten as

$$f_1 = \frac{q}{T}f_0\sum_n\sum_m \frac{J_nJ_m e^{i(n-m)\theta}}{w+i\nu-n\omega_c-k_z v_z}\left[(k_z v_z+n\omega_c)\Phi + i\nu\frac{n_1}{n_0}\frac{T}{q}\right]. \tag{A.8}$$

In the following calculations it is helpful to express the distribution function as $f_1 = A\Phi + Bn_1$, where

$$\begin{aligned} A &= \frac{q}{T}\frac{n_0}{\pi v_t^3}\sum_n\sum_m e^{i(n-m)\theta}F_\perp(v_\perp)A(v_z), \\ B &= \frac{q}{T}\frac{n_0}{\pi v_t^3}\sum_n\sum_m e^{i(n-m)\theta}F_\perp(v_\perp)B(v_z), \\ F_\perp(v_\perp) &= J_n\left(\frac{k_\perp v_\perp}{\omega_c}\right)J_m\left(\frac{k_\perp v_\perp}{\omega_c}\right)e^{-v_\perp^2/v_t^2}, \\ A(v_z) &= \frac{1}{\sqrt{\pi}}\frac{k_z v_z+n\omega_c}{\omega+i\nu-n\omega_z-k_z v_z}e^{-v_z^2/v_t^2}, \\ B(v_z) &= \frac{i}{\sqrt{\pi}}\frac{\nu T}{qn_0}\frac{1}{\omega+i\nu-n\omega_z-k_z v_z}e^{-v_z^2/v_t^2}. \end{aligned}$$

We immediately notice that the velocity distribution depends on $n_1 (= \int f_1 d^3\mathbf{v})$, which itself depends on f_1. However, since n_1 is not a function of velocity we can express it as

$$n_1 = \frac{\int A d^3\mathbf{v}}{1-\int B d^3\mathbf{v}}\Phi, \tag{A.9}$$

$$\text{where } \int d^3\mathbf{v} = \int_0^{2\pi}d\theta\int_\infty^\infty v_\perp dv_\perp\int_\infty^\infty dv_z \tag{A.10}$$

which upon combining with the Poisson equation produces the dispersion equation

$$k^2 - \frac{q}{\epsilon_0}\frac{\int A d^3\mathbf{v}}{1 - \int B d^3\mathbf{v}} = 0, \tag{A.11}$$

where $k^2 = k_\perp^2 + k_z^2$. The rest of this section is dedicated to evaluating the integrals in Eq. (A.11). Integrating both A and B over the angle θ allows the following contractions,

$$\begin{aligned}
\int_0^{2\pi} d\theta e^{i(n-m)\theta} &= 2\pi\delta(n-m) \\
A &= \frac{2qn_0}{T}\frac{1}{v_t^3}\sum_n F_\perp(v_\perp)A(v_z), \\
B &= \frac{2qn_0}{T}\frac{1}{v_t^3}\sum_n F_\perp(v_\perp)B(v_z), \\
F_\perp(v_\perp) &= J_n^2\left(\frac{k_\perp v_\perp}{\omega_c}\right)e^{-v_\perp^2/v_t^2}.
\end{aligned}$$

Next we integrate over $v_\perp$,

$$\int_\infty^\infty v_\perp dv_\perp F_\perp(v_\perp) = \frac{1}{2}v_t^2 e^{-\mu} I_n(\mu),$$

where $\mu = k_\perp^2 v_t^2/2\omega_c$, and $I_n(\mu)$ is the modified Bessel function of the first kind. Integration over v_z is a bit more complicated

$$\begin{aligned}
\int_\infty^\infty dv_z A(v_z) &= -v_t[1 + \xi_0 Z(\xi_n)], \\
\int_\infty^\infty dv_z B(v_z) &= -\frac{i\nu T}{qn_0 k_z} Z(\xi_n), \\
\text{where} \quad \xi_n &= \frac{\omega + i\nu - n\omega_c - k_z v_z}{k_z v_t}, \\
\text{and} \quad Z(\xi_n) &= \int_\infty^\infty \frac{e^{-z}dz}{z - \xi_n}.
\end{aligned}$$

Combining all integrals and summing over all charged species (ions and electrons) we obtain,

$$1 + \sum_s \alpha_s \frac{1 + e^{-\mu_s}\xi_{0s}\sum_n I_n(\mu_s)Z(\xi_{ns})}{1 + i(\nu_s/k_z v_{ts})e^{-\mu_s}\sum_n I_n(\mu_s)Z(\xi_{ns})} = 0, \tag{A.12}$$

where $\alpha_s = 1/k^2\lambda_{\mathrm{D}s}^2$ and $\lambda_{\mathrm{D}s}$ is the Debye length. It could be easily checked that upon setting all collision frequencies to zero Eq. (A.12) reduces to the familiar collisionless electrostatic dispersion relation, e.g. Eq. (85) given by Stix in Ref. [21].

Bibliography

[1] F. Skiff, F. Anderegg, and M.Q. Tran. Stochastic particle acceleration in an electrostatic wave. *Phys. Rev. Lett.*, 58(14):1430, April 1987.

[2] J. Goree, M. Ono, and L. K. Wong. Observation of the backward electrostatic ion-cyclotron wave. *Phys. Fluids*, 28(9):2845, September 1985.

[3] G.A. Goree. *The backward electrostatic ion-cyclotron wave, fast wave current drive, and fir laser scattering.* Ph.d, Princeton University, 1985.

[4] A. Fasoli, F. Skiff, and M.Q. Tran. Study of wave-particle interaction from the linear regime to dynamical chaos in a magnetized plasma. *Phys. plasmas*, 1(5):1452, May 1994.

[5] R. Sudit and F. F. Chen. Rf compensated probes for high-density discharges. *Plasma Sources Sci. Technol*, 3:162–168, 1994.

[6] J.G.Laframboise. Technical Report 100, University of Toronto, Institute for Aerospace Studies, 1966. Document No. AD634596.

[7] F.F.Chen, J.D. Evans, and D.Arnush. A floating potential method for measuring ion density. *Phys.Plasmas*, 9(4):1449, April 2002.

[8] D.E. Smith, E.J. Powers, and G.S. Cladwell. Fast-fourier-transform spectral-analysis techniques as a plasma fluctuation diagnostic tool. *IEEE Trans. Plasma Sci.*, PS-1:261, December 1974.

[9] F. Skiff and F. Anderegg. Direct observation of plasma dielectric motion. *Phys. Rev. Lett.*, 59(8):896, August 1987.

[10] M. Sarfaty, S. De Souza-Machado, and F. Skiff. Direct determination of ion wave fields in a hot magnetized and weakly collisional plasma. *Phys. Plasmas*, 3(12):4316, December 1996.

[11] R.A. Stern and J.A. Johnson, III. Plasma ion diagnostics using resonant fluorescence. *Phys. Rev. Lett.*, 34(25):1548, June 1975.

[12] D. Hill, S. Fornaca, and M.G. Wickham. Single frequency scanning laser as a plasma diagnostic. *Rev.Sci.Instrum.*, 54(3):309, March 1983.

[13] G.D. Severn, D.A. Edrich, and R. McWilliams. Argon ion laser-induced fluorescence with diode lasers. *Rev.Sci.Instrum.*, 69(1):10, January 1998.

[14] J.L. Kline. *Slow Wave Ion Heating and Parametric Instabilities in the HELIX Helicon Source.* Ph.d, West Virginia University, 2002.

[15] E. Scime, C. Biloiu, C. Compton, F. Doss, D. Venture, J. Heard, E. Choueiri, and R. Spektor. Laser induced fluorescence in a pulsed argon plasma. *Rev. Sci. Instrum. 76, 026107 (2005)*, 76:026107, 2005.

[16] G. D. Conway, A. J. Perry, and R. W. Boswell. Evolution of ion and electron energy distributions in pulsed helicon plasma discharges. *Plasma Sources Sci. Technol.*, 7:337, 1998.

[17] D.J. Strozzi, A.K. Ram, and A. Bers. Coherent acceleration of magnetized ions by electrostatic waves with arbitrary wavenumbers. *Phys. Plasmas*, 10(7):2722–2731, March 2003.

[18] S. Alba, G. Carbone, M. Fontanesi, A Galassi, C Riccardi, and E. Sindoni. Stochastic particle acceleration in an electrostatic wave. *Plasma Phys. Controlled Fusion*, 34(2):147, 1992.

[19] E. Y. Choueiri. Anomalous resistivity and heating in current-driven plasma thrusters. *Phys. Plasmas*, 6(5):2290, May 1999.

[20] E. Y. Choueiri. Instability of a current-carrying finite-beta collisional plasma. *Phys.Rev.E*, 64:066413, November 2001.

[21] T.H. Stix. *Waves in Plasmas.* Springer-Verlag, New York, 1992.

[22] R.W. Motley and N. D'Angelo. Excitation of electrostatic plasma oscillations near ion cyclotron frequency. *Phys. Fluids.*, 6(2):296, February 1963.

[23] M.Ono and K.L. Wong. Externally launched ion bernstein wave in the act-1 toroidal device. *Phys.Rev.Lett.*, 45(13):1105, September 1980.

[24] R.H. Neynaber, S.M. Trujillo, and E.W. Rothe. Symmetric-resonance charge transfer in ar from 0.1–20 ev using merging beams. *Phys.Rev.*, 157(1):101, May 1967.

[25] A.V. Phelps. The application of scattering cross sections to ion flux models in discharge sheaths. *Phys.Rev. Lett.*

[26] C. Biloiu, X. Sun, E. Choueiri, F. Doss, E. Scime, J. Heard, R. Spektor, and D. Ventura. Evolution of the parallel and perpendicular ion velocity distribution function in pulsed helicon plasma sources obtained by time resolved laser induced fluorescence. *To be published in Physics of Plasmas*, , pages = ,.

[27] J.L. Kline. Resonant ion heating in a helicon plasma. Ms, West Virginia University, 1998.

[28] J. Kline, E. Scime, P.A. Keiter, M.M. Balkey, and R.F. Boivin. Ion heating in the helix helicon plasma source. *Phys.Plasmas*, 6(12):4767–4772, December 1999.

[29] C.F.F. Karney. Stochastic ion heating by a lower hybrid wave. *Phys.Fluids*, 21(9):1584, September 1978.

[30] D. Benisti, A.K. Ram, and A. Bers. Ion dynamics in multiple electrostatic waves in a magnetized plasma. I. Coherent acceleration. *Phys. Plasma*, 5(9):3224, September 1998.

[31] D. Benisti, A.K. Ram, and A. Bers. Ion dynamics in multiple electrostatic waves in a magnetized plasma. II. Enhancement of the acceleration. *Phys. Plasma*, 5(9):3233, September 1998.

[32] C.F.F. Karney and A. Bers. Stochastic ion heating by a perpendicularly propagating electrostatic wave. *Phys. Rev. Lett.*, 39:550, 1977.

[33] C.F.F. Karney. Stochastic ion heating by a lower hybrid wave:ii. *Phys.Fluids*, 22(11):2188, November 1979.

[34] E.E. Scime, P.A Keiter, M.W. Zintl, M.M. Balkey, J.L Kline, and M.E. Koepke. Control of ion temperature anisotropy in a helicon plasma. *Plasma Sources Sci. Technol.*, 7:186, 1998.

[35] J.P. Dougherty. The conductivity of a partially ionized gas in alternating electric field. *J. Fluid Mech.*, 16:126, November 1963.

[36] E. Kreyszig. *Advanced Engineering Mathematics*. John Wiley, 8th edition, 1999.